

2004

Spontaneous pulse formation in bistable systems

George A. andrews

College of William & Mary - Arts & Sciences

Follow this and additional works at: <https://scholarworks.wm.edu/etd>



Part of the [Mathematics Commons](#), and the [Optics Commons](#)

Recommended Citation

andrews, George A., "Spontaneous pulse formation in bistable systems" (2004). *Dissertations, Theses, and Masters Projects*. Paper 1539623432.

<https://dx.doi.org/doi:10.21220/s2-q8tf-y551>

This Dissertation is brought to you for free and open access by the Theses, Dissertations, & Master Projects at W&M ScholarWorks. It has been accepted for inclusion in Dissertations, Theses, and Masters Projects by an authorized administrator of W&M ScholarWorks. For more information, please contact scholarworks@wm.edu.

SPONTANEOUS PULSE FORMATION IN BISTABLE SYSTEMS

A Dissertation

Presented to

The Faculty of the Department of Applied Science

The College of William and Mary in Virginia

In Partial Fulfillment

Of the Requirements for the Degree of

Doctor of Philosophy

by

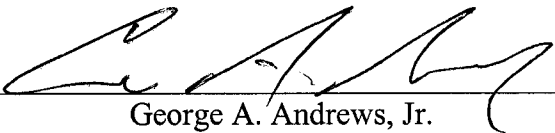
George A. Andrews Jr.

2004

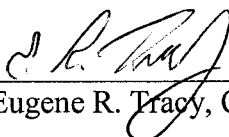
APPROVAL SHEET

This dissertation is submitted in partial fulfillment of
the requirements for the degree of

Doctor of Philosophy


George A. Andrews, Jr.

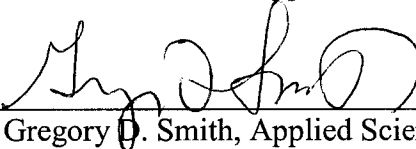
Approved by the Committee, December 5, 2003


Eugene R. Tracy, Chair


William E. Cooke, Physics


Roy L. Champion, Physics


Dennis M. Manos, Applied Science


Gregory D. Smith, Applied Science

DEDICATION

This dissertation is dedicated with loving gratitude to my life's companion Denise and to our four magnificent children: George, Michael, Michelle and Douglas.

CONTENTS

Acknowledgements	vi
List of Figures	ix
Abstract	x
1 Introduction	2
2 Model Development	9
3 Derivation of the Input-Output Models	18
3.1 The Transfer Maps	22
3.2 The Input-Output Relationship	24
4 1-D Fast Maps	28
4.1 1D Map on Intensity	33
4.2 1D Map Bifurcation Analysis	35
4.3 Co-dimension Two Unfolding	40
5 Slow Saturation Dynamics	46
5.1 Fixed Points of the Slow Medium Map	48
5.2 Stability of the Pulse Train	49
6 Memory Effects: Heuristic Approach	54
6.1 New Dynamical Behavior Associated with Memory Effects	55
6.2 Stability Analysis	58
7 Conclusions	79

8 Appendix	80
8.1 Light and Matter	80
8.2 Map on Integrals and Fluence Code	87
8.2.1 Fixed point MATLAB function	94
BIBLIOGRAPHY	96
VITA	98

ACKNOWLEDGEMENTS

I lovingly acknowledge Denise; my spouse, friend and lover. Without her support and care, this Doctorate would not have been remotely possible. I am forever indebted to her for my education and my happiness. I also thank my four children who have sacrificed and given so that I may pursue my goals; especially Michelle and Douglas, who were still under my care while I pursued my degree.

I offer my deepest gratitude and respect to my very capable adviser, Dr. Gene Tracy. It was Dr. Tracy's creativity and intelligence that spawned this research and whose wise and scholarly mentorship provided me the requisite guidance I sought in returning to school. I esteem Gene as a respected friend. I would also like to acknowledge Mr. Dennis Weaver for his warm friendship that served as invaluable personal support and for providing insight and poignant comment at the many working meetings.

I also gratefully acknowledge Dr. William Cooke and his graduate student Wei Yang, for expertly providing guidance and the crucial experimental results that served to guide our modeling endeavors. I also acknowledge and thank the faculty and staff of both The Applied Science and The Physics Departments at The College of William and Mary for attracting and supporting me. My career and my person have been greatly effected to the positive by both of these fine departments.

Finally, I wish to express my thanks to The Department of Energy and The Virginia Space Grant Consortium for their financial support in this effort.

LIST OF FIGURES

1.1	CPM laser time series containing drop-out.	3
2.1	Schematic of CPM laser.	10
2.2	Relevant time scales (not to scale)	11
2.3	Transfer factors	13
2.4	Cavity arrangement (not to scale) for uni-directional pulse.	14
2.5	Pulse formation via mode-locking.	15
3.1	Inversion number plots for a narrow Gaussian pulse for class A and B lasers. Solutions for (3.9) for $(\gamma_{11}, c_2) = (1,1)$ and $(\gamma_{11}, c_2) = (0.5,1)$ are given in blue and green, respectively; the solution for (3.11), with $a = 1$, is in red.	21
3.2	Inner and outer regions of the pulse train.	22
3.3	Characteristic curves for Maxwell-Bloch equation for the radiation field. Note that σ is a ray label while s is a parameter along the ray.	25
3.4	Boundary conditions for Maxwell-Bloch equation for the radiation field.	26
4.1	Fixed points for gain map.	30
4.2	Loss map.	32
4.3	Intensity maps (not to scale).	34
4.4	Critical surfaces for fixed point equation (4.15).	37

4.5	Pitchfork bifurcation: $R = 0.98$, $l = 0.04$ and $\theta = 1.33$	39
4.6	Saddle-node bifurcation: $R = 0.98$, $l = 0.05$ and $g = 0.06$	40
4.7	Generic saturation functions.	41
4.8	Generic transfer factor and fixed point equation.	42
4.9	Generic bifurcation diagram depicting the high-dimensional bifurcation point for the generic map.	43
4.10	Critical surfaces for the generic transfer factor (gray-scale) and the full map truncated to cubic order (multi-colored. The gain cap (red) is also included.	45
5.1	Localized intensity function and fluence.	50
5.2	Delta collapse.	52
6.1	Inner and outer regions of the pulse train.	56
6.2	Plot of (6.13) under bistable conditions.	58
6.3	5d Saddle-Node.	59
6.4	Perturbative spectra.	61
6.5	Spectra showing period two flip orbits and breathing oscillations.	61
6.6	Phase space after the occurrence of the Hopf bifurcation.	62
6.7	Time series revealing unstable oscillations after the Hopf bifurcation.	63
6.8	Experimental time series showing drop-out and drop-in data in arbitrary amplitude units for two, counter-propagating pulses.	63
6.9	Experimental time series showing drop-out, drop-in and overshoot phenomena.	64
6.10	Experimental time series for a single, uni-directional pulse.	64
6.11	Experimental time series.	65
6.12	Experimental time series showing chaotic-like instability.	66

6.13	Experimental time series showing asymmetry between counter-propagating pulses.	67
6.14	Suggestive phase portrait for linearized system with $\beta = 0$ depicting hysteresis in drop-out and drop-in phenomena.	68
6.15	Phase portrait around saddle showing period-two oscillations.	70
6.16	Same trajectories as Figure (6.15) but with period-two oscillations removed.	71
6.17	Numerical phase portrait for reduced system (6.19) under bistable conditions.	71
6.18	Rotated view of Figure (6.17).	72
6.19	Cartoon of manifold intersection.	73
6.20	Magnified view of numerical sampling around manifold intersection.	73
6.21	Time series (6.19) for fluence.	74
6.22	Time series (6.19) for saturation integral.	74
6.23	Phase portrait just before saddle-node bifurcation.	75
6.24	Time series just before saddle-node bifurcation.	75
6.25	Trans-critical bifurcation fixed point equation.	76
6.26	Phase space just before trans-critical bifurcation.	77
6.27	Rotated view of Figure (6.26).	77
6.28	Third view of Figure (6.26).	78

ABSTRACT

This thesis considers localized spontaneous pulse formation in nonlinear, dissipative systems that are far from equilibrium and which exhibit *bistability*. It is shown that such pulses can form in systems that are dominated by the combined effects of: 1) a saturable amplifying or *gain* region, 2) a saturable absorbing or *loss* region, and 3) cavity effects. Analysis is based upon novel models for both an inertialess material in which the absorber responds instantaneously and inertial material in which there is temporal delay in the response. Additionally, we include the situation where the material does not fully relax between pulses, i.e. *memory effects*. The results are shown to be generic but direct application is made to pulse formation and stability as observed and exploited in a colliding pulse mode-locked (CPM) dye laser in which the saturable gain and absorber are spatially localized. Bifurcation from a steady, pulsing state to one of several possible other states (laser *dropout* phenomena) is observed to occur in these systems and will also be addressed. Key results arising from the inclusion of memory effects are as follows: the existence of highly degenerate bifurcation scenarios, implying hysteresis-like behavior in drop-out/drop-in transitions; damped period-two oscillations; and much lower frequency damped oscillations—reminiscent of *breathing modes*.

SPONTANEOUS PULSE FORMATION IN BISTABLE SYSTEMS

CHAPTER 1

Introduction

This dissertation introduces new phenomenological models that describe the global dynamics associated with spontaneous pulse formation in bistable systems. Such pulse formation is routinely found to occur in optical systems. In particular, the type of pulse formation considered here is a passive consequence of the combined effects of a non-linear (saturable) amplifying material and a saturable absorber coupled together within an optical cavity. Optical pulses arise because of a self-selection and locking of a subset of neighboring cavity modes brought about by the nonlinearity of the materials. This phenomena is referred to as *passive mode locking* and has been the subject of great interest for several years (see [1, 2]). The global effect of mode locking is the transformation of the system state from one characterized by stochastic undulation of the numerous cavity modes to a highly ordered state characterized by steady-state pulsation. As such, the pulses resulting from this type of pulse formation constitute self-organized nonlinear structures that are sometimes referred to as *autosolitons* or *solitons* in the literature [3, 4, 5, 6, 7].

The models developed in this thesis are generic to systems possessing the above ingredients but particular focus will be on the formation and dynamics of optical pulses found in *colliding pulse mode locked dye* (CPM) lasers of the type regularly used by the Physics Department of The College of William & Mary. It is well known that CPM lasers undergo sudden changes of state where the pulsation either ceases altogether (*i.e.*, no lasing occurs) or the laser operates in a continuous-wave (CW) mode. This cessation of lasing is often referred to as laser *drop-out*; Figure (1.1)

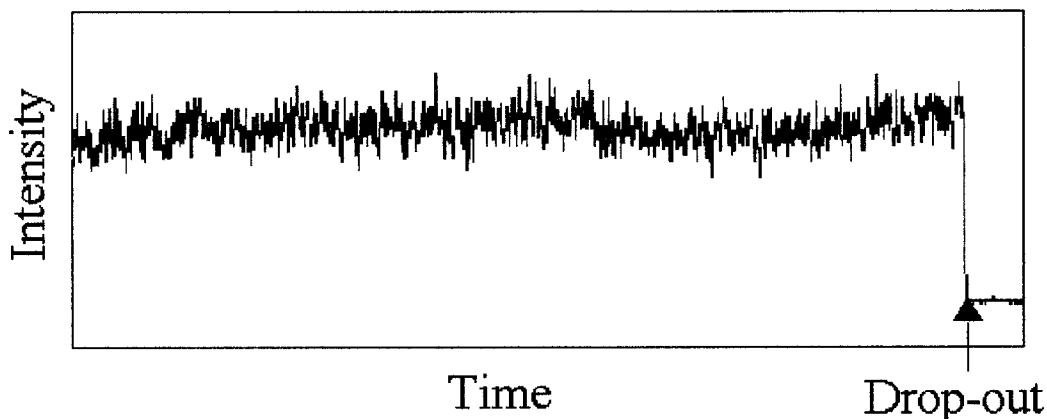


Figure 1.1: CPM laser time series containing drop-out.

reveals data in which such an event occurred as recorded from William & Mary's CPM laser. These systems are also known to spontaneously resume lasing as well; a phenomena we will refer to as laser *drop-in*. It is a key result of this work that the models predict the existence of an asymmetry or hysteresis between the dynamics of pulse formation and pulse cessation and that this prediction has been experimentally confirmed. Additionally, the models predict the existence of a high frequency period two oscillation, as well as slower *breather modes*, but these phenomena have not been experimentally observed to date.

Although the physics of CPM lasers is a mature field, the efforts thus far typically have adopted a *first principles* approach that has produced high fidelity but computationally complex models [1, 8, 9]. Consequently, these models are difficult or impossible to utilize in real-time control algorithms. In contrast, the long term goal of this modeling effort is to provide computationally efficient control laws that reproduce the global dynamics of the system to an adequate level of fidelity. It is anticipated that such control-laws can then be used for real-time time-series analysis, affording the potential for forecasting pending state changes or what we shall

call *bifurcation prediction*. It is, as it were, this middle ground in modeling that constitutes this effort's uniqueness. Consequently, a phenomenological approach has been adopted here in that experimental results have been heavily relied upon in guiding the model development. We show in this work that the dual requirements of computational efficiency and physical fidelity are satisfied by models in which only the combined effects of the following physical ingredients are included:

1. a *saturable* amplifying medium (*gain*);
2. a *saturable* absorbing medium (*loss*);
3. cavity effects.

The inclusion of more complex physical phenomena, such as dispersion, finite gain bandwidth, and the well known nonlinear Kerr or self-phase modulation, would indeed increase fidelity with regard to information on pulse shape but at a cost of computational efficiency; thus, for the purpose of control, we initially model amplitude dynamics and defer such model enhancements to future efforts.

Another key result of the work presented in this thesis is an increased understanding of the role of pulse-to-pulse *memory effects*—defined here as incomplete relaxation in the gain and/or loss material between pulses. That is, after the passage of a pulse through the material, there remains a residual population of the excited or ground states within the amplifying or absorbing material, respectively, which couples to the subsequent pulse. We emphasize that this incomplete relaxation is to be distinguished from the so called *slow media* models found in the optics literature. In these latter models, it is assumed that relaxation times of the materials are long when compared with the pulse width (hence *slow*)—but the absorber and gain are assumed to completely relax back to their initial state between pulses [1, 10]. The inclusion of memory effect as defined in this thesis, results in the following predictions:

1. slow amplitude *breathing* oscillations that occur after a change of state;
2. the existence of highly degenerate bifurcation scenarios, leading to hysteresis in the *drop-out/drop-in* cycles.

The breathing state listed above is predicted by the models to occur within physically realizable regimes in the parameter space; the highly degenerate bifurcation scenarios lead to the prediction of hysteresis-like behavior when the system transitions between drop-out and drop-in state changes and the reverse. Of the above predictions, 2. has been empirically observed in the CPM laser presently in use in the Physics Department at The College of William & Mary [11].

Of course, the addition of pulse-to-pulse memory effects necessarily increases the complexity of the model class. Without memory, the global dynamics on amplitude (and therefore intensity) is faithfully captured using simple nonlinear mappings that are discrete in time. When memory is included however, the resulting nonlinear model becomes a continuous (high-dimensional) integro-delay equation involving the pulse's integrated intensity—or the *fluence*—thereby introducing the notion of *saturation integrals*. As is fully discussed below, in some cases we are able to take advantage of the inherent stiffness of these saturation integrals and transform the integro-delay equation back into a discrete map. However, instead of amplitude or intensity serving as the dependent variables as in the maps without memory, the new map describes the dynamics of the saturation integrals and the *fluence*.

The analytical techniques adopted in this thesis are of course dictated by the mathematical characteristics inherent in the governing equations. In particular, the governing equations for our models exhibit the following important features:

1. Nonlinearity; since the full saturability of the materials is included.
2. Feedback and temporal delay; arising from the coupling effects of the cavity.

3. Stiffness; there exists multiple time scales over which the pulse dynamics occur.

The multiplicity of time scales listed above arises from the inclusion of memory since material relaxation times are comparable to the cavity round-trip time but are approximately five orders of magnitude greater than the pulse width.

The general methods and techniques of dynamical systems theory have been adopted to analyze the models and arrive at the results. Accordingly, the methodology of analysis consists of ascertaining steady-state solutions of the models (*i.e.*, the *fixed* points) and then varying system parameters to reveal the subsequent dynamics. Since the fixed points correspond to points in the parameter space where the system exhibits steady state behavior (both stable and unstable), the establishing of any change in the value or number of these fixed points as a result of parameter variation constitutes the most basic characterization of the system dynamics. In particular, a coalescence or disappearance of the fixed points (*i.e.*, a topological change in the attractors of the system) is called a *bifurcation* and indicates a dramatic change in the dynamical state of the system. Additionally, the parameter dependences for which such bifurcations occur, provides a direct opportunity for empirical verification of the models.

In optical systems where the key ingredients of saturable gain, absorber and cavity effects are found, the saturable media may be either spatially localized—as in the CPM lasers considered here—or spatially distributed in the form of crystals or optical fibers [12, 1, 8]. A model for such a distributed system that is related to our maps on amplitude and intensity has recently been proposed by Malomed *et. al.* [4]. However, in addition to the difference of Malomed's model possessing an extended absorber, it is further distinguished from our models in that Malomed examines transverse mode structure whereas our models describe one-dimensional longitudinal dynamics on pulse amplitudes and intensities. The increased complexity of our

models with the inclusion of memory presents sufficient challenge; restriction to one-dimension keeps the analysis tractable.

The methodology adopted in this work is heuristic as well as phenomenological and has been inspired by that of Haus [13]; but unlike Haus' treatment, we do not perform a small amplitude expansion on the saturable nonlinearities inherent in the material. Instead, we retain the full saturable forms for both absorber and amplifier. Moreover, as mentioned above, we also include pulse-to-pulse memory effects in a novel fashion. Further differences will be discussed as the model is fully developed below. Theoretical support and justification for our models is also achieved by a detailed derivation of their mathematical form from a two-level Maxwell-Bloch model. However, it should be kept in mind that the Maxwell-Bloch treatment is also phenomenological. We believe the methodology adopted here, *i.e.*, the development of a model that includes the complexities associated with pulse-to-pulse memory effects—and yet is simple enough to allow complete analysis—is our primary contribution.

The outline of the thesis is as follows: We begin Section 2 by expounding upon some of the ideas introduced above and separate the models into three distinct classes according to the material's response to the presence and passage of a pulse. We introduce the central notion of *transfer factors* to capture these responses and present the generic mathematical structure of the models by utilizing the transfer factors to form input-output relationships. Such a relationship is established first for each of the individual components of the physical system—an approach similar to that of New and Wilhelmi [8, 1]—with the full model then constructed by coupling the elements together in an optical cavity to form a closed loop. This introduces the important ingredients of feedback and delay into the model. Section 3 derives the the transfer factors used in the fast map models from the Maxwell-Bloch equations for two atomic level materials. In Section 4, we then introduce our discrete maps on the

dynamical variables of amplitude and intensity for the simplest of the three model classes involving an inertia-less or *fast absorber* that possesses no memory. This class of material response assumes that the atomic inversion levels are instantaneously created in response to the presence of a pulse and that they completely relax before the arrival of the next pulse. Sections 4.2 and 4.3 present the bifurcation analysis of these *fast maps*. We then introduce an inertial material that is still memoryless in Section 5 with subsequent analysis in sections 5.1 and 5.2, where we derive the result that bistable systems with slow media generate pulse trains spontaneously. To our knowledge, this result is new. In Section 6, we address memory effects first in a heuristic manner by low-pass filtering the saturation dynamics. This converts the discrete fast map of the inertialess material into a high dimensional integro-delay equation involving saturation integrals. Section 6.1 recovers a low-dimensional discrete map by taking advantage of the multiple time scales inherent in the system. This results in the final model that describes the dynamics of the saturation integrals and the integrated energy density (the *fluence*). Bifurcation analysis of this new system is performed in Section 6.2. Finally, summary and conclusions are drawn in Section 7 and derivation from first principles of the Maxwell–Bloch equations is provided in the Appendix. Also provided in the Appendix are the MATLAB codes used to generate the bifurcation plots and the stable and unstable manifolds.

CHAPTER 2

Model Development

As mentioned in the Introduction, we adopt a phenomenological approach by developing our models in close contact with observations made on a CPM laser presently in operation in the Physics Department of The College of William & Mary. The configuration and components of this laser are depicted schematically in Figure (2.1), which shows the laser configured in a ring-type geometry. The complete list of components found in this laser include localized regions of saturable gain and saturable loss provided by organic dye jets, and an array of prisms to correct for group velocity dispersion (GVD). Inversion in the gain jet is maintained by pumping the gain with a separate laser external to the system.

As further discussed below, CPM lasers derive their name from the well known fact that they optimize their output by superposing *counter propagating* pulses in the saturable absorber. However, since many quantitative aspects of the CPM dynamics are already present in the single unidirectional pulse mode, we restrict ourselves in this thesis to the *single-pulse* case. Focusing upon a single pulse also allows the key modeling issues to be identified more easily and, as will become evident, the single-pulse model possesses rich dynamical structure on its own accord. Given the present goal of understanding the global dynamics associated with *pulse formation* as opposed to effects upon *pulse shape*, the requirement of modeling simplicity suggests that we initially focus upon the combined iterated effects of the saturable gain and saturable absorber alone. As we show in Section 5, the effects of these two ingredients alone for slow media, when combined within a cavity,

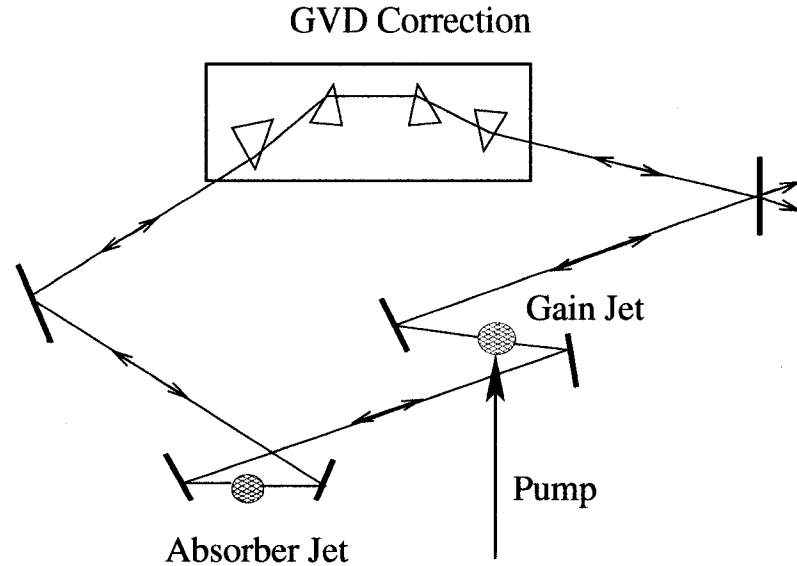


Figure 2.1: Schematic of CPM laser.

are sufficient to initiate pulse formation. Questions regarding pulse shape clearly require the inclusion of dispersion, finite gain bandwidth and self-phase modulation (*e.g.*, the Kerr effect), but these questions are postponed to future efforts. We also postpone the treatment of transverse dynamics and the influence of noise. As will be discussed, these simplifications are justifiable for systems exhibiting multiple time scales and where *global* information is all that is required to ascertain if pulse formation occurs. Indeed, for real-time control, pulse-to-pulse observations are at least highly desirable, and may be necessary. Additionally, at the high repetition rates found in CPM lasers, a single global quantity—such as the integrated intensity or *fluence*—is all that is readily accessible to measurement.

The development of our models capitalizes upon the multiple dynamical time scales inherent in the CPM laser. These temporal scales are notionally depicted in Figure (2.2). They include the period of the carrier signal that is on the order of 10^{-14} s; the pulse width on the order of $\Delta t \sim 10^{-13}$ s; and the cavity round trip time that is given by $\tau = L/c$, where L is the path length and c the speed

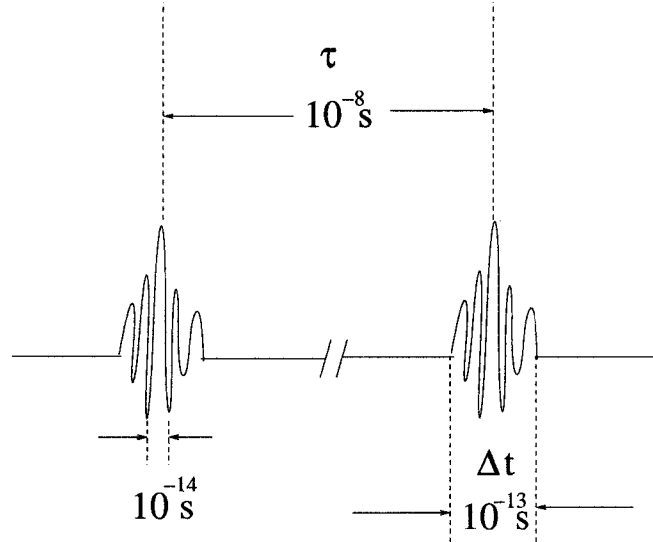


Figure 2.2: Relevant time scales (not to scale)

of light. For the laser under consideration here, $\tau \sim 10^{-8}s$. Additionally—and key in the consideration of memory effects—the dynamical time scales associated with population of the absorbing and amplifying material are observed to also be on the order of the round-trip time. For our purposes of developing control laws that govern pulse-to-pulse dynamics, these time scales further suggest that we focus upon the dynamics of the amplitude of the envelope function of the electric-field Ψ ; thus, defining the direction of propagation to be along the z -axis in a Cartesian coordinate system, we write the complex electric-field with a fixed polarization \hat{e} as

$$\mathbf{E}(z, t) = \Psi(z, t) \exp(i(kz - \omega t)) \hat{e} + \text{c.c.} \quad (2.1)$$

In (2.1), ω is 2π times the carrier frequency and $k = 2\pi/\lambda$ where here λ is the carrier wavelength; c.c. denotes complex conjugation.

The modeling approach adopted here entails developing *input-output* relations to characterize the presumably weak effects of the absorber and gain upon the pulse after a single pass. Toward this end, we account for these material effects by

introducing saturable *transfer factors* denoted by $f_{g,l}(\cdot)$ for each of the two materials. These transfer factors relate the amplitude of the pulse as it emerges from the material, Ψ^{out} to that of the pulse just prior to its entry, Ψ^{in} and should depend upon the energy (or equivalently, the square of the modulus of the amplitude) of the pulse in such a way so as to insure saturability. Consequently, we write the generic form of the input–output relations as

$$\Psi^{out} = f_{g,l}(|\Psi^{in}|^2)\Psi^{in}. \quad (2.2)$$

The situation is graphically depicted in Figure(2.3); note that $f_{g,l}(|\Psi|^2)$ might be a functional (*i.e.*, involve the history of $|\Psi|^2$, not just its instantaneous value).

One can think of these transfer factors as playing an analogous role to *transfer functions* as found in linear signal theory. In particular, from linear theory, the generic form of an input–output relationship is the convolution

$$\Psi^{out}(t) = h(t) * \Psi^{in}(t) = \int_{-\infty}^0 h(\xi)\Psi^{in}(t - \xi)d\xi, \quad (2.3)$$

where the kernel $h(\xi)$ contains the material's effects upon the pulse for $\xi \leq t$. Thus, Fourier transforming (2.3) produces the familiar transfer function

$$\hat{h}(\omega) = \frac{\hat{\Psi}^{out}(\omega)}{\hat{\Psi}^{in}(\omega)}, \quad (2.4)$$

where \hat{h} indicates Fourier transform of $h(t)$, *etc.*.

The particular forms of the transfer factors for our models were initially introduced in a heuristic manner. However, theoretical support is provided in the following section of the thesis by deriving the transfer factors from the semi–classical, two–level (atomic) Maxwell–Bloch equations. These well–known equations model the interaction of light with matter and are themselves derived from a more fundamental description in the Appendix.

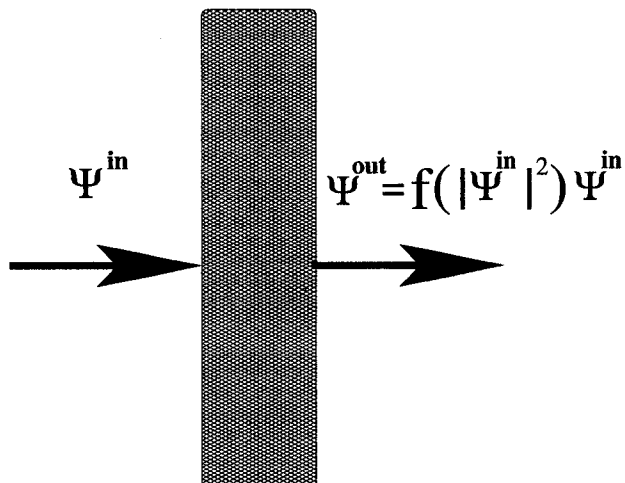


Figure 2.3: Transfer factors

As mentioned above, we focus here upon the dynamics associated with a unidirectional single pulse. Nevertheless, in anticipation of including a second counter-propagating pulse in the future, we introduce cavity effects by arranging the gain and loss media within the cavity as shown in Figure (2.4). Mode locking (pulse formation) occurs within such an arrangement when the system self-selects a group of cavity modes out of the numerous modes that constitute the initially stochastic non-lasing cavity state. A pulse forms when a particular noise spike has sufficient energy in its leading edge to saturate the absorbing material, thereby rendering the absorber transparent to the remainder of the fledgling pulse. This then allows the selected mode to enter the gain material where it undergoes amplification by stimulated emission and depletes the inverted levels. As a consequence of this depletion, the neighboring modes are inhibited from experiencing further gain. Figure (2.5) graphically illustrates this process for a pulse moving to the right where blue signifies low intensities that occur at the leading and trailing edges due to the saturable absorber and gain, respectively. This process repeats itself until the evolving pulse achieves a steady state—characterized for our purposes by a constant ampli-

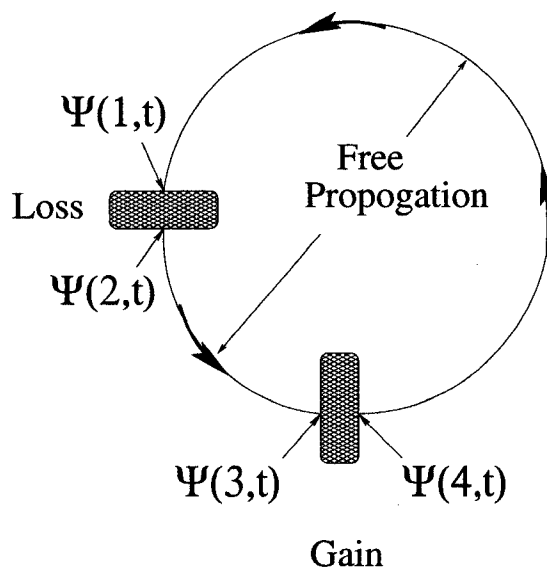


Figure 2.4: Cavity arrangement (not to scale) for uni-directional pulse.

tude spike. For the colliding pulse mode-locked laser, the simultaneous formation of a counter-propagating pulse occurs in an identical fashion; but in this multiple pulse mode, the absorption is ultimately reduced by the superposition of both pulses within the absorbing material. Such superposition minimizes loss per pulse; thereby enhancing pulse growth. Colliding pulse mode-locked lasers derive their name from this effect. Additionally, the configuration displayed in Figure (2.4) also affords maximal time for the gain material to recover between pulses via the external optical pump.

We incorporate these cavity effects by considering the amplitude of the signal's envelope function at the four entry and exit locations bracketing the absorber and the gain, indicated by $\Psi(i, t)$, $i \in \{1, 2, 3, 4\}$ in Figure (2.4). The dye jets within the cavity possess thicknesses on the order of tens of microns. Therefore, recalling that the cavity length is on the order of meters, we can ignore the time spent by the pulse within the dyes. While this time is negligible here, this simplification needs to be reconsidered for extended media; *e.g.*, in solid state lasers or fibers. Between the

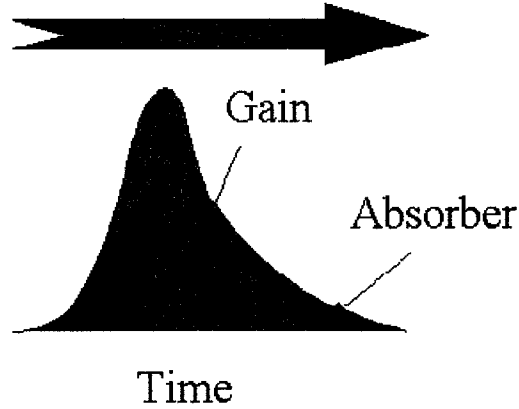


Figure 2.5: Pulse formation via mode-locking.

material regions, the pulse amplitude is assumed to propagate freely in the cavity without dispersion. With the choice of these cavity positions, $\Psi(z, t)$ can now be considered a discrete function of space when evaluated at these points.

In addition to coupling the effects of the gain and loss media, the cavity arrangement in Figure (2.4) also introduces feedback and temporal delay into the system. We incorporate these latter features into our models in the following manner: first we choose as our origin the position where the pulse first enters the absorber or loss, labeled as $\Psi(1, t)$ in Figure (2.4) and denote the round-trip time to be τ in arbitrary temporal units. With this choice of origin, it is deduced from the figure that a counter-clockwise pulse experiences free propagation for $\tau/4$ and $3\tau/4$ units (annotated as *free propagation* in the figure). Then, since we ignore the time the pulse spends inside the material, we relate the exiting pulse to the entering pulse for each material using equation (2.2) with the appropriate transfer factor as follows:

$$\begin{aligned} \text{loss transfer} &\Rightarrow \Psi(2, t) = f_l (|\Psi|^2(1, t)) \Psi(1, t), \\ \text{free propagation} &\Rightarrow \Psi(3, t + \tau/4) = \Psi(2, t), \end{aligned}$$

$$\begin{aligned}
\text{gain transfer} &\Rightarrow \Psi(4, t + \tau/4) = f_g(|\Psi|^2(3, t + \tau/4)) \Psi(3, t + \tau/4), \\
\text{free propagation} &\Rightarrow \Psi(1, t + \tau) = \Psi(4, t + \tau/4).
\end{aligned} \tag{2.5}$$

We then iterate, relating the envelope function of a pulse at the $(n+1)$ 'th round-trip to that at the n 'th by an appropriately *combined* transfer factor to be fully discussed below.

The above relations introduce a temporal lag equal to the round trip time τ into the map for each iteration n ; thus, we denote $\Psi(1, \tau) \mapsto \Psi^{(1)}$, and $\Psi(1, 2\tau) \mapsto \Psi^{(2)}$, *etc.*. To couple the material effects for a single circuit, the two single-element transfer factors are mathematically composed to form a *composite transfer factor*, $f(\cdot) \equiv (f_g \circ f_l)(\cdot)$, that acts upon a single pulse once per round trip. Due to the small gain/loss per pass (for the CPM laser this change is measured to be on the order of a few percent), we note that $(f_g \circ f_l)(\cdot) \approx (f_l \circ f_g)(\cdot)$. Consequently, denoting the system's parameters by λ , we arrive at a single circuit *map on amplitude*: $\Psi(1, t + \tau) = f(|\Psi|^2; \lambda) \Psi(1, t)$; or,

$$\Psi^{n+1} = F(|\Psi^n|^2; \lambda), \tag{2.6}$$

where

$$F(\Psi^n; \lambda) \equiv f(|\Psi^n|^2; \lambda) \Psi^n. \tag{2.7}$$

Initial data $\Psi^0(t)$ is assumed given. Since we are neglecting linear dispersion and self phase modulation (SPM), we observe in passing that the dynamics of the phase of Ψ , ϕ , is trivial; *i.e.*, $\phi^{n+1} = \phi^n$. Additional effects upon the phase result from the inclusion of noise. However, as mentioned in the introduction, we leave such non-trivial effects as a topic for future work.

In the next section, we derive the transfer factors that define the *fast maps* on amplitude and intensity for inertialess material from the Maxwell-Bloch equations.

This assumption of instantaneous response serves to simplify the underlying concepts and analyses and introduces necessary notations and ideas derived from nonlinear system and bifurcation theory. We also discuss the limitations of this class of models before moving on to inertial materials defining *slow maps* possessing pulse-to-pulse memory effects.

CHAPTER 3

Derivation of the Input-Output Models

In this section we motivate the transfer factors for fast materials by relating them to the atomic occupation levels within the materials. To this end, we utilize the well known Maxwell–Bloch equations that describe the (quantum) dynamics of the density matrix elements associated with energy level transitions that are stimulated by the presence of a pulse within the material. Following Newell [9], we refer to the occupation densities as *inversion numbers*.

The Maxwell-Bloch equations constitute a semi-classical approach to modeling the interaction of light with matter in that the density matrix elements of statistical quantum mechanics are related to the macroscopic polarization field variable associated with the materials as shown in the Appendix (see equation (8.18)). The polarization then couples to the cavity field through the classical Maxwell’s equations. We define a *fast medium* to be the case where the material is considered inertialess in that it responds instantaneously to the presence of a pulse. This assumption permits one to adiabatically eliminate the polarization and population density fields of the media by *slaving* them to the radiation field as discussed below. The result is a Lorentzian functional form for the population density analogous to the gain and loss transfer functions introduced heuristically in Section 4. Under the additional assumption of small effects per pass, it is shown here that the Maxwell-Bloch equations produce the input–output relation of the form examined through this thesis (see equation (2.6)).

Derivation of the Maxwell–Bloch equations from more basic principles is pro-

vided in the Appendix. Hence, for the purposes of this section, we begin by writing the equations down in the notation of Newell and Maloney [9] with the exception that we substitute $\Psi(\mathbf{r}, t)$ for their $A(\mathbf{r}, t)$ to represent the unidirectional, singly polarized radiation field envelope function. The full Maxwell-Bloch model for a two atomic level system is

$$(\partial_z + \frac{1}{c}\partial_t)\Psi = \frac{ic}{2\omega}\partial_x^2\Psi - \frac{\kappa}{c}\Psi + \frac{i\omega}{2\epsilon_0 c}\Lambda, \quad (3.1)$$

$$\partial_t N = -\gamma_{11}\Delta N + \frac{i2}{\hbar}(\Psi^*\Lambda - \Psi\Lambda^*), \quad (3.2)$$

$$\partial_t \Lambda = -\gamma_{12}\Lambda - i(\omega_{12} - \omega)\Lambda + \frac{ip^2}{\hbar}\Psi N; \quad (3.3)$$

where, $\Delta N \equiv (N - N_o)$, $i = \sqrt{-1}$, p is the magnitude of the dipole matrix element and $\kappa \equiv \sigma/\epsilon_o$. σ is the (finite) conductivity of the material, R is the reflectivity of the mirrors, c is the group velocity in the material, ϵ_o is the permittivity and L is the length between mirrors. Following Newell, $\omega_{12} \equiv \omega_1 - \omega_2$ is taken to be positive; *i.e.*, the energy level of atomic level 1 is greater than level 2. The inversion number N is an occupation density defined by equation (8.26) in the Appendix as $N = n_a(\rho_{22} - \rho_{11})$ and has the units of inverse volume. Thus, $N < 0 \Rightarrow$ an amplifying medium and $N > 0 \Rightarrow$ an absorber. $\gamma_{11}N_o$ is the constant pump rate providing the inversion for an amplifier and equals 0 for an absorber. Finally, as defined in the Appendix, γ_{11} and γ_{12} represent homogeneous broadening rates for the population inversion and polarization fields, respectively. For the goals of the present analysis, we can ignore the linear losses associated with the material as well as transverse effects (*i.e.*, $\Psi(\mathbf{r}, t) \rightarrow \Psi(z, t)$); we also neglect cavity detuning. Consequently we set $\kappa = \partial_x^2\Psi = (\omega_{12} - \omega) = 0$ in the above equations.

The decay rate for the polarization field, γ_{12} , is known to be three orders of magnitude faster than that of the population density γ_{11} ([1, see table on page 31]). Consequently, we can simplify the Maxwell-Bloch system by slaving the polarization

field variable to the inversion number. Mathematically, this allows the temporal derivative in (3.3) to be ignored and results in the algebraic relation:

$$\Lambda = i \frac{p^2}{\hbar\gamma_{12}} \Psi N. \quad (3.4)$$

This result defines *class B* lasers. For fast media, the population density can also be slaved to the radiation field in equation (3.2) to define *class A* lasers. Under these assumptions, the temporal derivative in (3.2) can be set to zero so that

$$N = N_0 - i \frac{2}{\hbar\gamma_{11}} (\Psi^* \Lambda - \Psi \Lambda^*), \quad (3.5)$$

where $(\cdot)^*$ denotes complex conjugation. Thus, combining equations (3.4) and (3.5)—with $N \in \mathbb{R}$ —results in an inversion function that is Lorentzian in its dependence upon the intensity:

$$N = \frac{N_0}{1 + \frac{4p^2}{\hbar^2\gamma_{12}\gamma_{11}} |\Psi|^2}. \quad (3.6)$$

This result will be utilized in the transfer factor for the gain map later defined in (4.2). From (3.6), we see that the saturation coefficient a (introduced in (4.2)) is related to the physical parameters inherent in the Maxwell-Bloch model by

$$a \equiv \frac{4p^2}{\hbar^2\gamma_{12}\gamma_{11}}. \quad (3.7)$$

Returning to class B lasers, inserting (3.4) into (3.2) results in a two dimensional system [6]:

$$\left(\partial_z + \frac{1}{c} \partial_t \right) \Psi = -c_1 N \Psi, \quad (3.8)$$

$$\partial_t N = \gamma_{11} N_0 - \gamma_{11} N + c_2 |\Psi|^2 N; \quad (3.9)$$

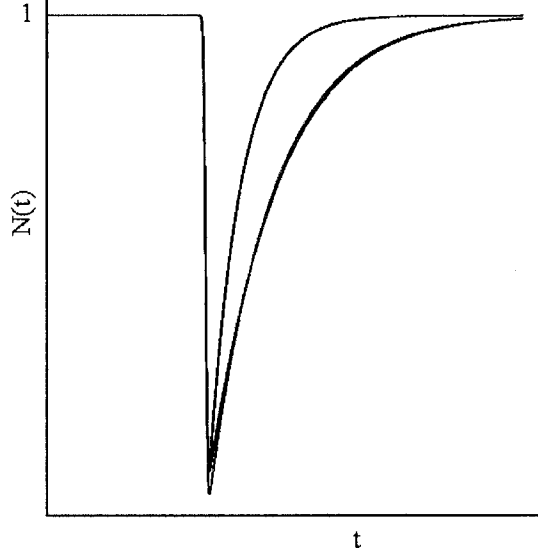


Figure 3.1: Inversion number plots for a narrow Gaussian pulse for class A and B lasers. Solutions for (3.9) for $(\gamma_{11}, c_2) = (1,1)$ and $(\gamma_{11}, c_2) = (0.5,1)$ are given in blue and green, respectively; the solution for (3.11), with $a = 1$, is in red.

where, $c_1 \equiv p^2\omega/2\epsilon_0\hbar\gamma_{12}$ with physical units of *area* and $c_2 \equiv -4p^2/\hbar^2\gamma_{12}$ having units of $1/(\text{Field}^2\text{time})$. For a narrow Gaussian pulse shape,

$$|\Psi|^2(t) = \frac{|\Psi_*|^2}{\sqrt{2\pi\Delta t^2}} e^{-\frac{(t-t_0)^2}{2\Delta t^2}}, \quad (3.10)$$

Figure (3.1) depicts the numerical solution of equation (3.9) for a class B laser at $z = 0$. Also shown in Figure (3.1) for comparison is the Lorentzian saturability curve associated with a class A laser having a *slow absorber* for the same Gaussian pulse shape of the form

$$N[|\Psi|^2] = \frac{1}{1 + aS_g[|\Psi|^2](z, t)}. \quad (3.11)$$

In (3.11), the material response is not instantaneous and is accounted for heuristically by the saturation integral, $S_g[|\Psi|^2](z, t)$, defined later by equation (5.1) (compare to (3.6)). As the figure reveals, the similarity between the two curves suggests

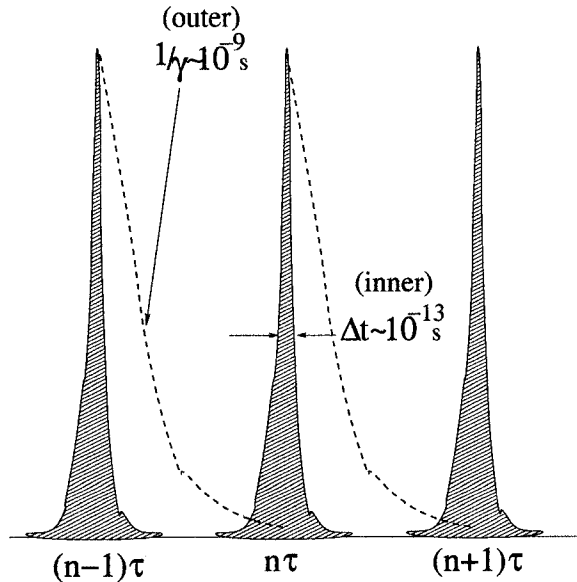


Figure 3.2: Inner and outer regions of the pulse train.

a robustness of the field dynamics to the form of the population density. This will be discussed in Section 6.

3.1 The Transfer Maps

In this section we provide a formal solution of the 2-d system describing the dynamics of a class B laser defined in the previous section by taking advantage of the multiple time scales inherent in the system. When a pulse is present, the material responds on a time scale dictated by the pulse width Δt ; however, after the passage of a pulse, the inversion number N in (3.9) relaxes back to its equilibrium value on the much longer time scale γ_{11}^{-1} (see Figure (3.2)). Such multiple time scales therefore suggest a singular perturbative approach as follows [14]:

First we analyze the system away from the pulse to obtain the *outer solution* by letting $\Psi \rightarrow 0$ in (3.8) and (3.9). In this limit, $N \rightarrow N_0$, the pump equilibrium—suggesting we scale both N to this constant $\tilde{N} \equiv N/N_0$ and the independent variable t to the relaxation rate $\tilde{t} \equiv \gamma_{11} t$. The natural spatial scale for the system is the length

of the material η , thus $\tilde{z} \equiv z/\eta$. Applying these scalings and suppressing explicit reference to the spatial dependence, the dimensionless *outer equation* that describes the dynamics of the material's response in the absence of the pulse becomes

$$\partial_{\tilde{t}} \tilde{N}^{(o)}(\tilde{t}) = 1 - \tilde{N}^{(o)}(\tilde{t}); \quad (3.12)$$

where, a tilde denotes a dimensionless quantity. In physical units, the solution of (3.12) is

$$N^{(o)}(t) = e^{-\gamma_{11}(t-t_o^{(o)})} (N^{(o)}(t_o^{(o)}) - 1) + 1. \quad (3.13)$$

where, $t_o^{(o)}$ is the temporal *boundary layer* where the outer solution is to be matched to the *inner solution* (determined below) and $N^{(o)}(t_o^{(o)})$ is a constant of integration that is also determined by the matching conditions.

To find the inner solution when the pulse is present, we maintain the spatial scaling as above, but now rescale time to the pulse width $\tilde{t} \equiv t/\Delta t$. In this limit, the dependent field variables are rescaled to their maximum or saturation values $\tilde{\Psi} \equiv \Psi/|\Psi_{sat}|$ and $\tilde{N} \equiv N/|N_{sat}|$. With these new scalings, the dimensionless *inner equations* are

$$\left(\partial_{\tilde{z}} + \frac{1}{\tilde{v}} \partial_{\tilde{t}} \right) \tilde{\Psi}(\tilde{z}, \tilde{t}) = -\tilde{c}_1 \tilde{N} \left[|\tilde{\Psi}|^2 \right](\tilde{z}, \tilde{t}) \tilde{\Psi}(\tilde{z}, \tilde{t}), \quad (3.14)$$

$$\partial_{\tilde{t}} \tilde{N}(\tilde{z}, \tilde{t}) = \tilde{\epsilon} \tilde{N}_o - \tilde{\epsilon} \tilde{N}(\tilde{z}, \tilde{t}) - \tilde{c}_2 |\tilde{\Psi}|^2(\tilde{z}, \tilde{t}) \tilde{N}(\tilde{z}, \tilde{t}); \quad (3.15)$$

where, $\tilde{c}_1 \equiv c_1 L N_{sat}$, $\tilde{c}_2 \equiv c_2 \Delta t |\tilde{\Psi}_{sat}|^2$, and $\tilde{\epsilon} \equiv \Delta t \gamma_{11}$; \tilde{v} is a dimensionless group speed that can be set to 1 with the appropriate choice of coordinate system and $\tilde{N}_o \equiv N_o/N_{sat} < 1$. In this limit, the nonlinear term on the right hand side of (3.15) $\sim \mathcal{O}(1)$ while the first two terms are $\mathcal{O}(\tilde{\epsilon}) \ll 1$. Thus, the inner equation is found

by ignoring the linear terms resulting in the inner solution for the inversion number (in physical units)

$$N^{(i)}(z, t) = N^{(i)}(z, t_o^{(i)}) \exp\left(-\tilde{c}_2 \int_{t_o^{(i)}}^t dt' |\tilde{\Psi}|^2(z, t')\right). \quad (3.16)$$

In (3.16), $t_o^{(i)}$ denotes the temporal boundary for the inner solution and $N^{(i)}(t_o^{(i)})$ is a constant of integration determined by the matching conditions. To match the inner and outer solutions, we introduce a time $t_b = \sqrt{\tau \Delta t}$ such that $\Delta t < t_b < \tau$. Thus the matching condition is formally found by evaluating $N^{(i)}(z, t_o^{(i)} = t_b) = N^{(o)}(z, t_o^{(o)} = t_b)$.

3.2 The Input–Output Relationship

In this section we derive the input–output relationship for $\tilde{\Psi}$, having solved the inner equation (3.15) for \tilde{N} by adopting a normal perturbative approach. We chose the amplifying medium and therefore write $\tilde{c}_1 \equiv -g$ in (3.14). Using the method of characteristics to transform (3.14) to an ODE, we integrate along a ray in space-time that we parametrized by σ as graphically depicted in Figure (3.3). The dynamical equation takes the form

$$\frac{d\tilde{\Psi}(s; \sigma)}{ds} = g\tilde{N}[|\tilde{\Psi}|^2](s; \sigma)\tilde{\Psi}(s; \sigma). \quad (3.17)$$

We denote s_0 and s_1 to be the lower and upper limits of integration, respectively, and note that $\{s_0, \sigma\}$ label the initial event corresponding to when and where the pulse enters the material, and $\{s_1, \sigma\}$ signifies the final space-time event when and where it leaves. Integration along a particular ray thereby produces

$$\tilde{\Psi}(s; \sigma) = \tilde{\Psi}(s_0; \sigma) + g \int_{s_0}^{s_1} ds' \tilde{N}[|\tilde{\Psi}|^2](s'; \sigma)\tilde{\Psi}(s'). \quad (3.18)$$

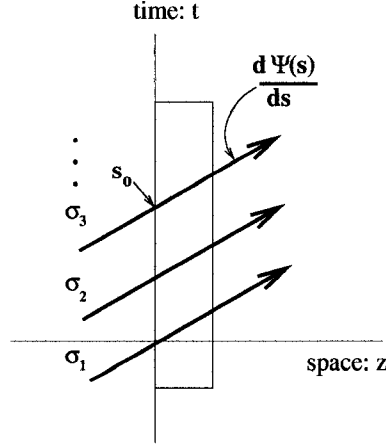


Figure 3.3: Characteristic curves for Maxwell-Bloch equation for the radiation field. Note that σ is a ray label while s is a parameter along the ray.

Incorporating the fact that both the absorber and gain only effect the pulse by a few percent in a single pass (recall $g \approx 1 - 2\%$), we perform a regular perturbation analysis in g as follows [14]: Suppressing explicit reference to σ for notational clarity, and expanding to leading order in g , (3.17) has the perturbative solution

$$\tilde{\Psi}(s) \cong \tilde{\Psi}_0(s) + g\tilde{\Psi}_1(s). \quad (3.19)$$

Thus, inserting this leading-order solution into equation (3.18) produces

$$\tilde{\Psi}_0(s) + g\tilde{\Psi}_1(s) \cong \tilde{\Psi}(s_0) + g \int_{s_0}^s ds' \tilde{N}[|\tilde{\Psi}_0 + g\tilde{\Psi}_1|^2](s') (\tilde{\Psi}_0(s) + g\tilde{\Psi}_1(s)). \quad (3.20)$$

The functional in the above integrand is further expanded to leading order, which upon equating terms according to powers of g , results in the following system (note that $\tilde{\Psi}(s_0) = \text{constant}$):

$$g^0: \tilde{\Psi}_0(s) = \tilde{\Psi}(s_0), \quad (3.21)$$

$$g^1: \tilde{\Psi}_1(s) = (s - s_0) \tilde{N}[|\tilde{\Psi}_0|^2] \tilde{\Psi}_0(s_0). \quad (3.22)$$

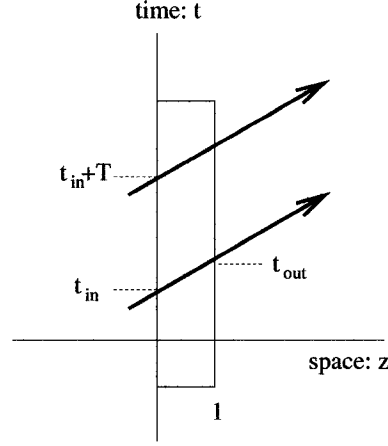


Figure 3.4: Boundary conditions for Maxwell-Bloch equation for the radiation field.

Equation (3.21) captures the free propagation of a pulse and (3.22) describes the first order perturbation of the pulse due to the dynamics associated with the inversion number \tilde{N} . Choosing $z=0$ to be a fiducial point where the pulse enters the jet implies $(s_0, \sigma) = (0, t_{in})$. The point where the pulse emerges from the material is then $(s_1, \sigma) = (1, t_{out})$ as shown in Figure (3.4). Thus, $(s - s_0) = 1$ in equation (3.22). Equation (3.19) consequently gives the perturbed solution

$$\tilde{\Psi}(1, t_{out}) = \left(1 + g\tilde{N}[|\tilde{\Psi}|^2](0, t_{in}) \right) \tilde{\Psi}(0, t_{in}), \quad (3.23)$$

which is the generic input-output relations we desire. Using either the Lorentzian saturation curve for a fast absorber defined by (3.6) or for a slow absorber defined by (3.11) for the functional $\tilde{N}[|\tilde{\Psi}|^2]$ produces the maps on amplitude (and intensity) to be analyzed in this thesis. In particular, the fast map on amplitude, or the *gain map*, is

$$\tilde{\Psi}(1, t_{out}) = \left(1 + \frac{g}{1 + \tilde{a}|\tilde{\Psi}|^2(0, t_{in})} \right) \tilde{\Psi}(0, t_{in}). \quad (3.24)$$

Similar arguments lead to an identical loss map on amplitude with $g \rightarrow -l$ and $a \rightarrow b$

where the saturation constant b is likewise related to physical parameters inherent in the Maxwell-Bloch model as in (3.7). The resulting *loss maps* are therefore

$$\tilde{\Psi}(1, t_{out}) = \left(1 - \frac{l}{1 + \tilde{b}|\tilde{\Psi}|^2(0, t_{in})}\right) \tilde{\Psi}(0, t_{in}). \quad (3.25)$$

CHAPTER 4

1-D Fast Maps

In this section, we adopt a heuristic approach (originally motivated by Haus [13]) in developing the one-dimensional discrete maps on pulse amplitude and intensity derived in Section 3.2 above. We focus here on class A lasers in that we consider the materials as inertialess and assume small single-pass material effects. Furthermore, the material is considered to instantaneously and completely relax after the passage of a pulse (*i.e.*, no memory effects). We refer to these models as *fast maps* without memory.

To begin, we assume an exponential transfer factor of the form

$$f(|\Psi^n|^2; c_1, c_2) \equiv \exp\left(\frac{c_1}{1 + c_2|\Psi^n|^2}\right), \quad (4.1)$$

where c_1 and c_2 are positive definite physical parameters whose values characterize the type of material as discussed in Chapter 3. For an amplifier $c_1 \equiv +g$ is the linear amplification factor and describes the linear *gain*; for linear *loss*, $c_1 \equiv -l$. The saturability parameters $c_2 \equiv a$ and $c_2 \equiv b$ control the relative saturation rates of the amplifier or an absorber, respectively. For the CPM laser in use at William & Mary, g is measured to be on the order of 10^{-2} , justifying the small gain per pass assumption and allowing expansion of (4.1) to leading order in g . To account for non-saturable losses due to scattering from material surfaces, mirrors, prisms, *etc.*, we must introduce an additional loss parameter $R < 1$ into the transfer factor defined by (4.1). In this work, R is taken to be ≈ 0.98 based on measured values.

Hence, with these definitions and assumptions, the transfer factor for the gain is explicitly given as

$$f_g(|\Psi^{in}|^2; a, g, R) \approx R \left(1 + \frac{g}{1 + a|\Psi^n|^2} \right). \quad (4.2)$$

When (4.2) is substituted into (2.6), the result is a one-dimensional map on pulse amplitude

$$\Psi^{n+1} = R \left(1 + \frac{g}{1 + a|\Psi^n|^2} \right) \Psi^n. \quad (4.3)$$

Equation (4.3) is the *gain map* defined in 3.24 and is recognized to be the discrete analogue of the *laser equation* [1, see equation (2.11)]. From equation (4.3), it is deduced that the map is dynamically stable when the magnitude of the transfer factor is less than or equal to one and unstable when it is greater than one. Referring to Figure (4.1), which plots Ψ^{n+1} against Ψ^n , unstable states result when the slope at the fixed point is greater than one, and stable states occur when the slope is less than one. For the special case where the transfer factor is unity, the amplitude does not change upon further iteration—signifying that the fixed point has neutral stability. The amplitude values under steady state conditions are the *fixed points* of the system and lie at intersections with the identity map as denoted in the figure. Consequently, simple analysis of (4.3) reveals that at threshold ($\Psi = 0$) the gain map has a slope equal to $R(1 + g)$. This is, therefore, the stability condition for the origin that imposes a constraint upon the values of the linear gain and reflective loss parameters, g, R . Thus, a necessary condition for lasing is

$$R(1 + g) > 1. \quad (4.4)$$

Further analysis of the gain map reveals the key role of saturability. The effects of saturation are clearly depicted in Figure (4.1) for the case of an unstable origin.

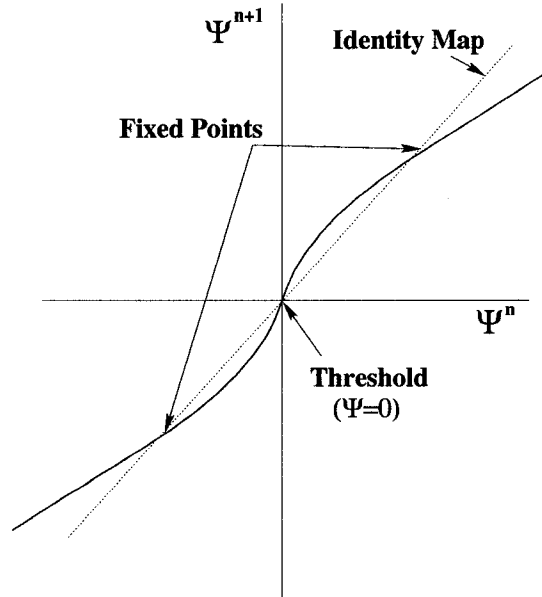


Figure 4.1: Fixed points for gain map.

It is seen in the figure, that as the amplitude grows, the saturability of the material causes the map to intersect the identity map at two points as it asymptotically approaches $R < 1$; *i.e.*, there is an appearance of two more fixed points in addition to the origin. However, unlike the origin, these new fixed points are stable. This scenario would not occur in the case of a stable origin.

In conclusion, analysis of (4.3) reveals that—when the system becomes unstable at threshold (*i.e.*, $f(\Psi = 0) > 1$ where $f(\cdot)$ is the transfer factor), the system produces additional stable fixed points for which $\Psi^{n+1} = \Psi^n$ in \pm pairs at non-zero amplitudes. This production of fixed points constitutes a topological change in the system's phase space relative to when the threshold is stable and thereby provides our first example of a bifurcation. The appearance and characterization (*i.e.*, stable or unstable) of such fixed points forms the method of analysis employed throughout this thesis. For the CPM laser, the physical interpretation of the fixed points associated with the gain map for an unstable origin is that they represent

stable continuous wave (CW) lasing.

For the absorber map, we follow the same procedure but now set $c_1 \equiv -l$ and $c_2 \equiv b$ in equation (4.1). For the CPM laser, l has also been measured to be on the order of a few percent. Thus, expanding the exponential to leading order in l , produces the loss transfer factor:

$$f_l(|\Psi^{in}|^2; b, l) \approx \left(1 - \frac{l}{1 + b|\Psi^n|^2}\right). \quad (4.5)$$

When substituted into equation (2.6), the resulting loss map is seen to be equation (3.25)

$$\Psi^{n+1} = \left(1 - \frac{l}{1 + b|\Psi^n|^2}\right) \Psi^n. \quad (4.6)$$

Equation (4.6) is plotted in Figure(4.2) where it is seen that a single stable fixed point exists at the origin where the slope is equal to $-l$. Furthermore, the amplitude asymptotes to a curve having constant slope below the identity map as shown in the figure. Thus, the nonlinear effect of saturation implies that at large amplitudes (or intensities), the absorber becomes *bleached*—rendering it nearly transparent.

To model the combined effects of both the absorber and the gain for a single pass, we form the *composite transfer factor* by composing (4.2) and (4.5),

$$f(\Psi) = f_g(f_l(\Psi)); \quad (4.7)$$

which, when substituted into (2.6), produces the *composite map*:

$$\Psi^{n+1} = R \left(1 + \frac{g}{1 + a \left(1 - \frac{l}{1 + b|\Psi^n|^2}\right)^2 |\Psi^n|^2}\right) \times \left(1 - \frac{l}{1 + b|\Psi^n|^2}\right) \Psi^n. \quad (4.8)$$

The parameter space is thus seen to be $\lambda \equiv \{a, b, g, l, R\}$, *i.e.*, $\lambda \in R^5$.

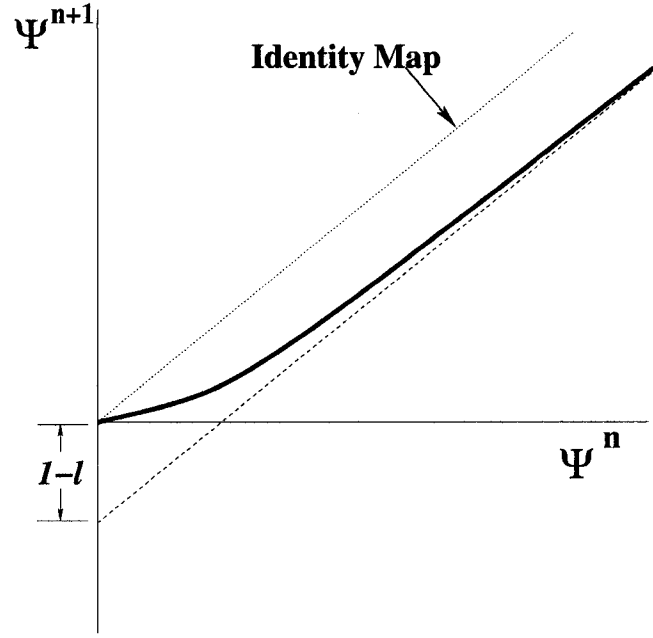


Figure 4.2: Loss map.

Bifurcation analysis of equation (4.8) similar to that presented for the gain and absorber maps just discussed (the full methodology is discussed below) has shown that we can simplify the composite map without significantly affecting the global dynamics for physically interesting parameter regions by expanding (4.8) to leading order in g, l ; *i.e.*, by neglecting terms of $\mathcal{O}(gl, g^2, l^2)$. This is consistent with the expansion of the individual exponential transfer maps to the same order. The result is an *additive transfer factor* that, when inserted into (2.6), produces an *additive map on amplitude*:

$$\Psi^{n+1} = R \left\{ 1 + \frac{g}{1 + a|\Psi^n|^2} - \frac{l}{1 + b|\Psi^n|^2} \right\} \Psi^n. \quad (4.9)$$

The nonlinearity in equation (4.9) is strikingly similar to that of the continuous model proposed by Malomed *et al.* for pulse propagation in optical waveguides [4]. It is important to note that the dynamics described by (4.9) are extremely stiff, with

the single-pass transfer factor differing from the identity map by only $\approx 10^{-3}$ over the entire operating range of amplitudes. However, although nonlinear effects are weak *per pass*, they have dramatic cumulative effects on the asymptotic behavior.

The form of equation (4.9) suggests that—in the absence of noise—we can scale the amplitude by an arbitrary constant, k ; i.e., $\tilde{\Psi} = k\Psi$ and absorb k into a and b . By choosing this constant to be \sqrt{a} , we can affect a reduction in the dimension of the parameter space such that, $\lambda = \{\theta, g, l, R\}$; i.e., $\lambda \in R^4$, where θ involves the ratio b/a . For plotting purposes, we form the relation $b/a \equiv \tan \theta$ to capture the entire range, $(b/a) \in [0, +\infty]$, for a finite range of $\theta \in [0, \pi/2]$. Dropping tildes, we consequently arrive at:

$$\Psi^{n+1} = R \left\{ 1 + \frac{g}{1 + |\Psi^n|^2} - \frac{l}{1 + \tan \theta |\Psi^n|^2} \right\} \Psi^n. \quad (4.10)$$

As will be discussed later, in a CPM dye laser, the ratio determining θ can be experimentally controlled by adjusting the beam diameters focused upon the dyes; and the parameter g is readily manipulated by increasing the pumping power of the argon laser. The loss parameters $\{R, l\}$, are not easily manipulated experimentally—but are not expected to vary much for a given experimental run (l changes as the dye ages, but is otherwise constant).

4.1 1D Map on Intensity

In this section we introduce the map on pulse intensity. However, we present here only a brief discussion of its associated dynamics in order to introduce the key concept of *bistability* and to introduce the methodology adopted in forthcoming detailed analysis. Defining the intensity of the pulse as

$$I^n \equiv |\Psi^n|^2, \quad (4.11)$$

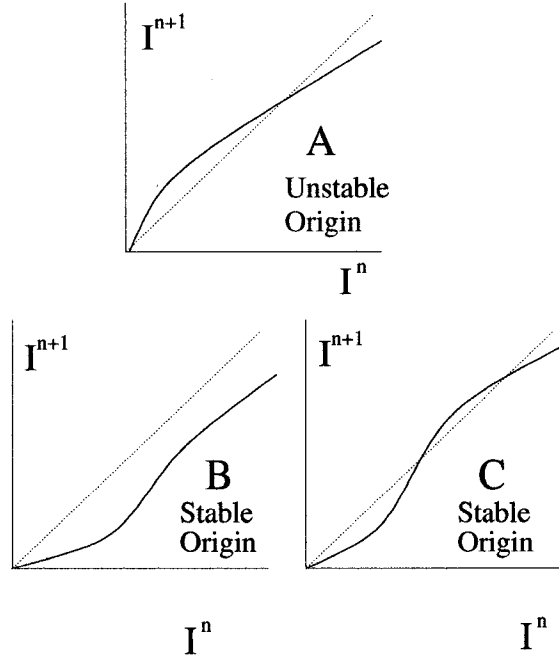


Figure 4.3: Intensity maps (not to scale).

we arrive at a discrete map on pulse intensity of the form: $I^{n+1} = f(I^n)I^n = F(I^n)$, by taking the modulus squared of both sides of (4.10) and keeping only terms of $\mathcal{O}(g, l)$. The new parameter values in this map are found to be simply related to the original parameters by: $\theta \mapsto \theta$, $g \mapsto 2g$, $l \mapsto 2l$ and $R \mapsto R^2$. The result is the following *map on intensity*:

$$I^{n+1} = R^2 \left\{ 1 + \frac{2g}{1 + I^n} - \frac{2l}{1 + \tan \theta I^n} \right\} I^n. \quad (4.12)$$

As in the gain map, the dynamics associated with the pulse intensity is ascertained by finding and characterizing the fixed points of (4.12). From (4.12), the fixed point equation for the intensity map is seen to have the form

$$(f(I) - 1)I = 0. \quad (4.13)$$

This equation reduces to a simple cubic polynomial in I whose zeros (one of which

is seen to be at threshold, $I = 0$) define the fixed points. Factoring out the origin leaves a quadratic equation whose zeros determine the remaining two fixed points. Since on physical grounds intensities are positive definite, the map is limited to the three possibilities displayed in Figure (4.3). (The plots in Figure (4.3) are meant for notional purposes only and are not to scale due to the stiffness inherent in the map). In the plots, the zeros of equation (4.13) are mapped to the intercept points on the identity map. As in the gain map plotted in Figure(4.1), Figure(4.3-A) shows that if the origin is unstable, only a single stable fixed point is possible. However, referring to Figure(4.3-C), it is seen that when the origin is stable, an unstable and another stable fixed point is possible. Under these conditions, the system exhibits the phenomena of *bistability*[15]. As we'll see, bistability is essential for pulse formation.

In the following sections, we analyze both the 1-D map on amplitude (4.10) and the intensity map (4.12) introduced in this section. We adopt this strategy since the intensity map offers a substantial simplification in the mathematics as compared to the map on amplitude but retains the global dynamical behavior of the latter. However, the map on amplitude is important to the future addition of physical effects that impact phase dynamics. Consequently, we shift between the two maps as required for continuity of discussion.

4.2 1D Map Bifurcation Analysis

In this section, we begin with the map on amplitude defined by equation (4.9). The methodology follows that outlined above for the map on intensity; *i.e.*, the fixed points are first determined as functions in the parameter space and then bifurcation scenarios are established.

Changing notation so that $\Psi \equiv x$ represents a constant real amplitude, the fixed point equation associated with (4.10) is again a rational function of the form:

$$(f(x; \lambda) - 1)x = 0; \quad (4.14)$$

where it is recalled that the parameter vector $\lambda \in \mathbb{R}^4$, and the transfer function $f(\cdot)$ is defined in (4.10). Upon clearing out the denominators and factoring out the root at threshold, the result is a quintic polynomial in x of the form:

$$\begin{aligned} x(\epsilon_5 x^4 + \epsilon_3 x^2 + \epsilon_1) &= 0, \\ \Rightarrow xP_4(x) &= 0; \end{aligned} \quad (4.15)$$

where, $P_4(x)$ is the quartic remainder in x and $\epsilon_i = \epsilon_i(\lambda)$ are parameter-dependent coefficients defined as

$$\begin{aligned} \epsilon_5 &= \tan \theta (R - 1), \\ \epsilon_3 &= R[(1 - l) + \tan \theta (1 + g)] - (\tan \theta + 1), \\ \epsilon_1 &= R(1 - l + g) - 1. \end{aligned} \quad (4.16)$$

Equation (4.15) is quadratic in x^2 with the discriminant defined by

$$\Delta(\lambda) \equiv \epsilon_5^2 \prod_{i \neq j} (x_j - x_i)^2. \quad (4.17)$$

Since the discriminant is an implicit function of the parameter set, the locus of parameter values $\{\lambda_i\}$ for which $\Delta(\lambda_i) = 0$ therefore defines a surface in the parameter space whose dimension is typically equal to one less than the number of parameters; *i.e.*, 3. Since this surface contains multiple branches upon which the roots of equation (4.15) are degenerate, it both identifies (experimentally verifiable) parameter sets for which bifurcations occur and separates the parameter space into dynamically distinct regions. We refer to this surface as the *critical surface*.

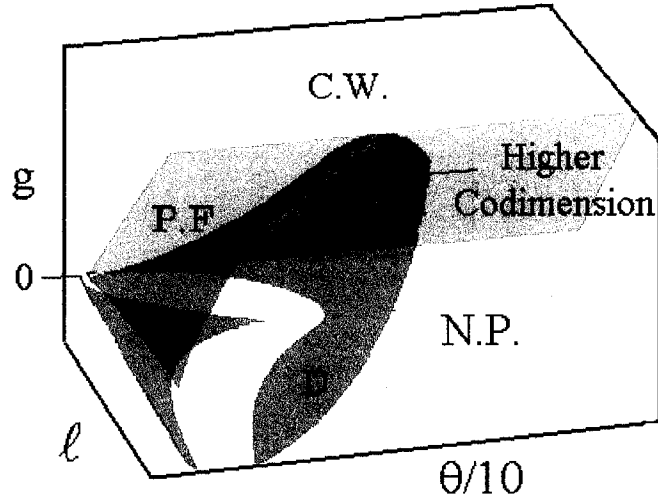


Figure 4.4: Critical surfaces for fixed point equation (4.15).

One of the branches of the critical surface is given by

$$\epsilon_1 = R(1 - l + g) - 1 = 0. \quad (4.18)$$

This equation plays the same role as equation (4.4) for the gain map. Consequently, we designate this branch as the *gain cap*, since given values for $\{R, l\}$ (recall these parameters can be considered as constants for a given experimental run) (4.18) implies the existence of a critical value of the gain g , for which the origin bifurcates from a stable point to an unstable one. Fixing R to 0.98, and using physically realistic ranges for $\{\theta, g, l\}$, we therefore generate the full critical surface as displayed in Figure (4.4). This figure was generated using Maple's 3-d implicit plot function on equation (4.17). In the figure, the θ axis has been arbitrarily scaled by a factor of 10 for visual clarity and G denotes the gain cap; the surface D will be discussed momentarily.

As mentioned in Section 4 (see Figure (4.3A)), when the region above the

gain cap has a single, stable fixed point, this can be interpreted as a continuous-wave mode of lasing; accordingly, this region is denoted by C.W. in Figure (4.4). Imaginary amplitudes occur for parameter values enclosed within the folded surface D, as well as to the right of D and below the gain cap; thus, these regions are interpreted to be non-physical and designated N.P. in Figure (4.4). To the left of surface D, and below the gain-cap, there exists a region labeled P.F.—indicating pulse formation. It is within this region that the system exhibits bistability; *i.e.*, the origin is stable and a second stable fixed point appears (see Figure (4.3C)).

Figure (4.4) displays the full physical range of $\theta = (0, \pi/2)$ with $\theta > \pi/2 \Rightarrow b/a < 0$. However, since on physical grounds both a and b are positive constants this region of the model is non-physical. Our model predicts that the amplitude of the fixed point increases in magnitude as $\theta \rightarrow \pi/2$; this agrees with both experiment and other models [1]. Also noted in the figure is a tangential intersection that occurs between two branches of the critical surface (*i.e.*, the gain cap and the surface labeled D). This intersection is a one-dimensional curve representing a family of parameter values for which higher *co-dimensional* bifurcations occur [16]. As is more fully discussed below, such increased co-dimensionality has important dynamical consequences in terms of the stability of a system when parameter values lie on or near this curve. It is noted that, Malomed *et. al.* [4] have also observed higher co-dimensional bifurcation scenarios in their work.

Figures (4.5) and (4.6) display plots of the map for the two, co-dimension-1 bifurcation scenarios associated with the G (gain cap) and D branch, respectively (also see Figures (4.3A) through (4.3C)). Normally, one plots $F(\Psi)$ vs. Ψ , but due to the extreme stiffness of these maps mentioned earlier, we plot $F(\Psi) - \Psi$ along the vertical axis to clearly show variation (recall, $F(\Psi) - \Psi \approx 10^{-3}$). Consequently, negative values of $F(\Psi) - \Psi$ denote regions where the amplitude is decreasing upon iteration and positive values indicate the converse; the zeros of $F(\Psi) - \Psi$ are the

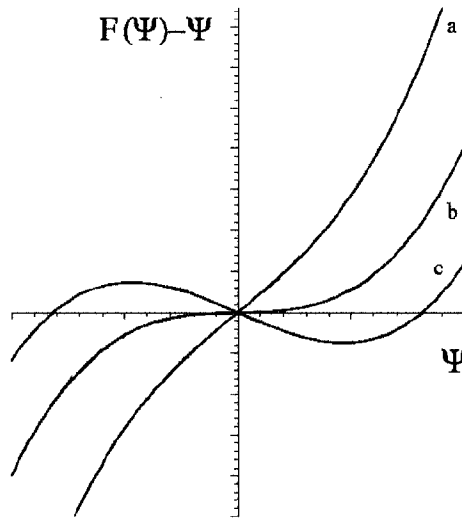


Figure 4.5: Pitchfork bifurcation: $R = 0.98$, $l = 0.04$ and $\theta = 1.33$.

fixed points.

Figure (4.5) illustrates a *pitchfork* bifurcation by showing curves for three different values of the gain parameter g (delineated in the figure by the annotation, a, b, c); the remaining parameters were set to $R = 0.98$, $l = 0.04$ and $\theta = 1.33$. The domain for the plots was selected so that the pitchfork nature of the bifurcation can be readily seen. The pair of stable fixed points located further from the origin (that survive the bifurcation) are also not displayed for clarity. When g is below its critical value, the system is located within the pulse formation (P.F.) region of Figure (4.4). The sequence $c \rightarrow b \rightarrow a$ of Figure (4.5) corresponds to moving from the P.F region of Figure (4.4) upwards through the gain cap G into the C.W. region.

Figure (4.6) shows plots for three different values of θ with $R = 0.98$, $l = 0.05$, $g = 0.06$. Only positive valued amplitudes are displayed. Bistability (implying pulse formation) is clearly seen for curve c . When the value of θ equals its critical value, Figure (4.6) shows the two fixed points become degenerate; the system resides on the D surface of Figure (4.4). Further decrease of θ results in the loss of bistability, but

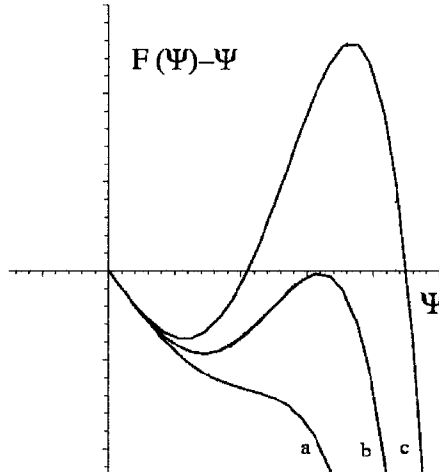


Figure 4.6: Saddle-node bifurcation: $R = 0.98$, $l = 0.05$ and $g = 0.06$.

the origin remains stable. This is therefore recognized as a *saddle-node* bifurcation. The sequence $c \rightarrow b \rightarrow a$ corresponds to moving in Figure (4.4) from the P.F. region to the right, passing through the critical surface and into the region marked D.

4.3 Co-dimension Two Unfolding

We now discuss the higher co-dimension bifurcation discovered in the fast maps and generalize the discussion by introducing a generic map that consists of unspecified saturable functions. As will be shown, the only requirement placed upon these functions is that they be monotonic. The key result of this generalization is that we can now consider pulse formation in a completely general framework affording application of our models to other physical systems than the CPM laser.

We relate the generic map to the CPM models by utilizing the map on intensity defined by equation (4.12). Accordingly, it is important to note that the higher co-dimension tangency found in (4.12) occurs where the pitchfork and saddle node coalesce. This implies that all of the fixed points are in the immediate vicinity of the origin allowing a Taylor series expansion of the nonlinearity about this root.

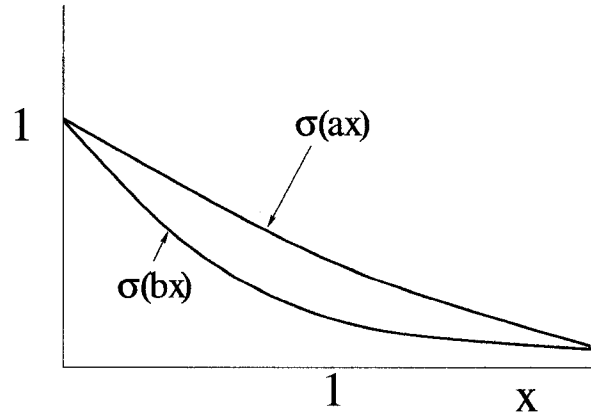


Figure 4.7: Generic saturation functions.

Thus we have

$$F(x) = f(x)x = (f(0) + f'(0)x + f''(0)x^2/2)x + \mathcal{O}(x^4). \quad (4.19)$$

Since this is the map on intensity, we have $x \sim I \sim |\Psi|^2$, making (4.19) 5th order in the amplitude. Note that if we truncate the expansion at a lower order, we lose the phenomenon of interest: the merging of all 5 roots. Away from the line of tangency in Figure (4.4), the Taylor expansion becomes invalid and we must retain the full saturable nonlinearity.

Introducing monotonically decreasing, bounded saturation functions that possess parametric dependencies of the form: $\sigma(ax)$, $\sigma(bx)$ (e.g. for Lorentzian functions, $\sigma(ax) = 1/(1 + ax)$), and stipulating $b > a$ so that the absorber saturates faster than the gain (see Figure (4.7)), we form a *generic transfer factor* of the form

$$f(x) = R^2 (1 + 2g\sigma(ax) - 2l\sigma(bx)). \quad (4.20)$$

Because of the construction of (4.20), certain parameter regimes imply the ex-

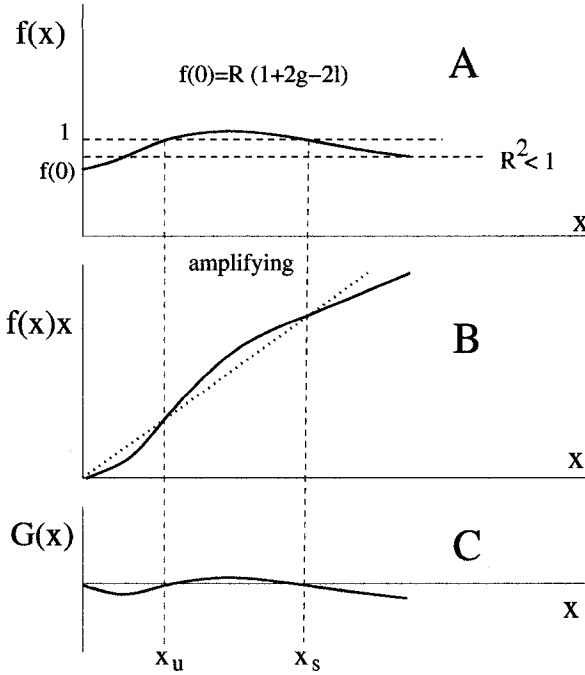


Figure 4.8: Generic transfer factor and fixed point equation.

istence of an amplifying subdomain over which $f(x) > 1$ as depicted in Figure (4.8A). Thus, the dynamics generated by a map utilizing equation (4.20) in this region of the parameter space will exhibit bistability. As mentioned above, higher co-dimensionality occurs in our system when the pitchfork and saddle-node bifurcations occur together (the tangential intersection of the branches in Figure (4.4)); this requires $f(x)$ to be at least quadratic in x to produce the requisite cubic (in x) fixed point equation $G(x) \equiv (f(x) - 1)x = 0$. Consequently, by expanding the generic transfer factor in equation (4.20) to second order, the generic fixed point equation becomes:

$$G(x) = (\epsilon_3 x^2 + \epsilon_2 x + \epsilon_1)x = 0; \quad (4.21)$$

$$\epsilon_1 = R^2(1 + 2g - 2l) - 1, \quad (4.22)$$

$$\epsilon_2 = R^2 \sigma'(0)(ag - bl), \quad (4.23)$$

$$\epsilon_3 = R^2 \sigma''(0)(a^2 g - b^2 l). \quad (4.24)$$

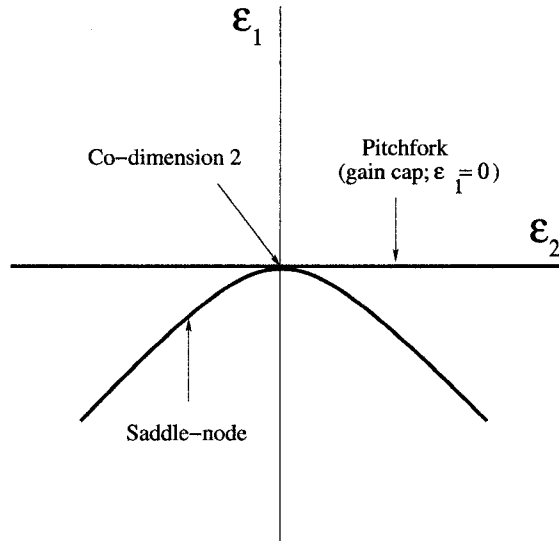


Figure 4.9: Generic bifurcation diagram depicting the high-dimensional bifurcation point for the generic map.

The general behavior required of $G(x)$ to exhibit bistability is graphically depicted in Figure (4.8C) where it is observed that a stable origin implies $G'(0) < 0$; or equivalently, $\epsilon_1 < 0$ in equation (4.22) as expected; thus, $\epsilon_1 = 0$ is our gain cap. Let's assume the origin is stable. Since $f(x)$ is parabolic and $f(0) < 1$, then for bistability, we require $f'(0) > 0$. Global stability requires $f(x)$ to be concave down, or $f''(0) < 0$. $f'(0) > 0$ implies $\epsilon_2 > 0$, giving $\sigma'(0) < 0$ in equation (4.23). The physical requirement for two positive, real valued roots (for $G(x) = 0$) implies $\epsilon_3 < 0$ since $f(x)$ must be concave down at $x = 0$. Finally, from the fact that $(g/l) \approx 1$ with $b > a$ by assumption, we deduce from equation (4.24) that $\sigma''(0) > 0$.

Since the co-dimension two bifurcations occur at points in the parameter space where there is full degeneracy among the roots, the locus of points for which the discriminant of the quadratic in (4.21) vanishes define the bifurcation values; *i.e.*, the parabola in parameter space defined by

$$\Delta = \epsilon_2^2 - 4\epsilon_3\epsilon_1 = 0. \quad (4.25)$$

Figure (4.9) is a schematic representation of the generic bifurcation diagram depicting a slice through the two-dimensional critical surface; *i.e.*, the (ϵ_2, ϵ_1) plane. Taking the magnitudes of $\sigma'(0)$ and $\sigma''(0)$ to be one, a supercritical pitchfork bifurcation occurs at the origin when ϵ_1 becomes positive as indicated in Figure (4.9); the saddle-node bifurcation surface is parabolic. In this coordinate system, the origin defines the point at which a co-dimension two bifurcation occurs; *i.e.*, this is where the tangential intersection of the two branches of the critical surface occurs.

To compare our map with the generic scenarios, we expand (4.15) to cubic order and transform to a coordinate system defined by the Taylor coefficients of the expansion (the *truncated model*). Figure (4.10) reveals critical surfaces for both this truncated model and the generic map associated with equation (4.8) for a section of parameter space that is consistent with the bistability requirements discussed above. Note that Figure (4.9) is a slice through Figure (4.10) for a particular ϵ_3 . The gain cap is also displayed in Figure(4.10) and constitutes the (ϵ_2, ϵ_3) plane. As the figure reveals, the truncated fast map exhibits a folded surface that is fully contained by the critical surface of the generic map. Consequently, the truncation of the generic map to cubic order captures the qualitative behavior of the higher co-dimensional bifurcation at threshold—though it predicts a smaller operating range for pulse formation.

This section concludes discussion on the inertialess models. While these fast maps have served to illuminate the dynamics in terms of amplitude stability, they have presumed the existence of a pulse as a consequence of an unstable origin (recall Figure (4.1)). They do not provide information on pulse formation. This limitation is a consequence of the lack of coupling between the temporal points which therefore

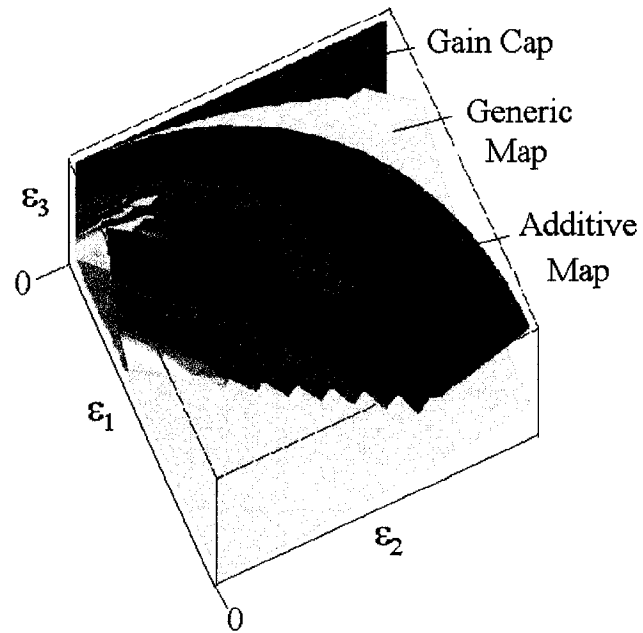


Figure 4.10: Critical surfaces for the generic transfer factor (gray-scale) and the full map truncated to cubic order (multi-colored). The gain cap (red) is also included.

evolve separately from each other, resulting in *boxcar-like* wave forms. To couple the neighboring points, one can include differential information or memory effects via integration over the pulse's history. The former has been thoroughly investigated by others (see for example [10, 1]) while we turn to the latter in the following sections.

CHAPTER 5

Slow Saturation Dynamics

In many systems the absorber and gain recovery times are on the order of the pulse round-trip time; hence, the need to consider pulse-to-pulse memory effects in these systems is apparent. Physical examples of such residual phenomena include lingering inversion densities in optical systems and *bump-on-tail* energetic particle distributions in confined plasmas. To account for these effects phenomenologically, we introduce the *saturation integrals*:

$$S_{g,l}(t) \equiv \int_{-\infty}^t K_{g,l}(t, t') |\Psi(t')|^2 dt'; \quad (5.1)$$

where, $K_{g,l}(t, t')$ represents response kernels for the gain and loss, respectively. A theoretical justification of this approach was given in Chapter 3.

The kernels $K_{g,l}$ should be thought of as *filters*. The stationarity of the system parameters requires that $K_{g,l}$ depend only on the difference $(t - t')$. We assume, on physical grounds, that $K_{g,l}$ are weighted toward the *recent past* and decay to zero as $t' \rightarrow -\infty$. There are three distinct classes of response kernels for $t > t'$ that we deal with separately:

- A) $K_{g,l} = \delta(t - t')$;
- B) $K_{g,l} = \mathcal{O}(1)$ for $(t - t') = \mathcal{O}(\Delta t)$ and $K_{g,l} = 0$ for $(t - t') = \mathcal{O}(\tau)$;
- C) $K_{g,l} = \mathcal{O}(1)$ for $(t - t') = \mathcal{O}(\Delta t)$ and $K_{g,l} = \mathcal{O}(1)$ for $(t - t') = \mathcal{O}(\tau)$ and $\int_{-\infty}^t K_{g,l}(t - t') = \kappa_{g,l} = \text{const.} < \infty$.

A is the class of *fast* maps already discussed. Class B consists of *slow* media, but the media has fully recovered between pulses. Class C consists of systems with pulse-to-pulse interactions. When these saturation integrals are inserted into the transfer factor of an input-output relation, the result is an infinite dimensional, integro-delay equation that describes the dynamics of a self-coupled pulse; *i.e.*, a map that now entails coupling of neighboring temporal points. Henceforth, we refer to this new map as the *slow medium map*:

$$\Psi(t + \tau) = f [|\Psi|^2] (t) \Psi(t). \quad (5.2)$$

To make the problem well-posed, initial data must be given for $\Psi(t)$, $-\infty < t < \tau$. A single iteration of (5.2) generates $\Psi(t)$, $\tau \leq t < 2\tau$, *etc.*. It is to be noted that our use of the word *slow* differs from its use in the optics literature; there, a slow absorber refers to the medium's response as compared to the pulse width while we imply pulse-to-pulse memory effects. In equation (5.2), $f[\cdot]$ denotes the functional:

$$f [|\Psi|^2] (t) \equiv R^2 \left(1 + \frac{2g}{1 + aS_g(t)} - \frac{2l}{1 + bS_l(t)} \right). \quad (5.3)$$

In the following section we begin by discussing the evolution of pulse shape for slow or *inertial* media—but in the absence of pulse-to-pulse memory effects, *i.e.* class B above. We then heuristically introduce memory by directly substituting the saturation integrals into the fast map (4.9). The main conclusion of this approach is that there is a minor shift in the parameter values for which pulse formation occurs—but the major bifurcation scenarios of the fast and slow maps (*i.e.*, saddle-node and pitchfork) remain qualitatively the same. We end with a more rigorous approach by taking advantage of the inherent singular nature of the system found in the widely separate temporal scales to reduce the ∞ -dimensional integral-delay equation to a low dimensional (*e.g.*, 3 or 5) map.

5.1 Fixed Points of the Slow Medium Map

Combining (5.2) and (5.3) explicitly reveals the slow medium map to be an *integro-delay* equation:

$$\Psi(t + \tau) = R^2 \left(1 + \frac{2g}{1 + aS_g(t)} - \frac{2l}{1 + bS_l(t)} \right) \Psi(t). \quad (5.4)$$

Following the procedures for analyzing maps and flows, we gain insight into the dynamics of (5.4) by considering fixed points and periodic orbits and their stability.

Fixed points: We require $\Psi(t) = \Psi_0 = \text{constant}$. This is true if $\Psi_0 = 0$, trivially. But, we also have (using the condition $\int_{-\infty}^t dt' K_{g,l}(t - t') = \kappa_{g,l}$),

$$\Psi_0 = R^2 \left(1 + \frac{2g}{1 + a\kappa_g \Psi_0^2} - \frac{2l}{1 + b\kappa_l \Psi_0^2} \right) \Psi_0. \quad (5.5)$$

Therefore, $\Psi_0 \neq 0$ implies

$$R^2 \left(1 + \frac{2g}{1 + a\kappa_g \Psi_0^2} - \frac{2l}{1 + b\kappa_l \Psi_0^2} \right) = 1. \quad (5.6)$$

Defining $a' = a\kappa_g$, $b' = b\kappa_l$, we recover the original fixed point equation of the fast map (4.9). Thus, Figure (4.4) still defines the critical surface for (5.4) but with $\tan\theta' = \kappa_l \tan\theta / \kappa_g$. We note that this is a CW solution.

Periodic orbits: Here we investigate the existence and nature of periodic orbits; *i.e.*, for a 'period-one' orbit, $\Psi(t + \tau) = \Psi(t)$ for all $-\infty < t < \infty$. A period-two orbit would satisfy $\Psi(t + 2\tau) = \Psi(t)$, *etc.* for period- n . We note that the periodicity condition

$$\Psi(t) = R^2 \left(1 + \frac{2g}{1 + aS_g(t)} - \frac{2l}{1 + bS_l(t)} \right) \Psi(t) \quad (5.7)$$

implies $\Psi(t) = 0$, or $R^2 \left(1 + \frac{2g}{1 + aS_g(t)} - \frac{2l}{1 + bS_l(t)} \right) = 1$. It is possible to show that solutions under these conditions will consist of δ -like pulse trains. More precisely,

$$|\Psi|^2(t) = |\Psi_*|^2 \sum_{n=-\infty}^{\infty} \delta(t - n\tau), \quad (5.8)$$

with $\Psi(t)$ an infinite train of *half-densities* (distributions whose square is a δ -function). In the next section, we consider the specific example for $S_{g,l}(t)$ provided by the Maxwell–Bloch model of Chapter 3.

5.2 Stability of the Pulse Train

To address stability of the pulse trains, while continuing to ignore memory effects, we set the response kernels in (5.1) to unity, but assume the media completely relax between pulses (class B above). Based upon the phenomenon of mode-locking discussed in the Introduction, the net effect of the amplifying and absorbing media is a reduction of the pulse width. Recall that mode-locking is a consequence of a saturable absorber preferentially removing the leading edge of a pulse, while a saturable gain preferentially amplifies the pulse peak—effectively removing the trailing edge of the pulse (see Figure (2.5)). Hence, without dispersive or nonlinear self-phase modulation effects to balance this narrowing (such as GVD or nonlinear-Kerr in optics), any initial pulse shape is therefore expected to asymptotically collapse into a delta function. As a consequence, it is anticipated that pulse formation will result in a delta-like pulse.

We can construct a pulse train solution to (5.4) by writing the intensity in terms of functions $\phi_i(t)$, such that $\{\phi_i(t) : I(t) \equiv |\Psi|^2(t) = \sum_{n=-\infty}^{+\infty} |\phi_i|^2(t - n\tau)\}$. These functions are of finite support with the width of each $|\phi_i|^2(t)$ assumed to be much less than the round trip time. Thus the integrated intensity for a single pulse becomes:

$$\Phi_i(t) \equiv \int_{-\infty}^t |\phi_i|^2(t') dt'. \quad (5.9)$$

In the optics literature, equation (5.9) is known as the *fluence*. Due to the finite

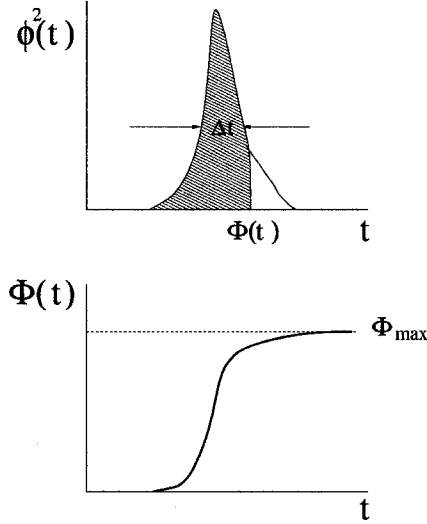


Figure 5.1: Localized intensity function and fluence.

support of $\phi(t)$, the fluence evaluates to a maximum Φ_{max}^n when integrated across the n^{th} pulse as depicted in Figure (5.1). Since differentiating the fluence recovers the intensity, $I(t)$, we can define a *functional map on intensity* of the form,

$$\frac{d\Phi^{n+1}(t)}{dt} = f(\Phi^n(t)) \frac{d\Phi^n(t)}{dt}; \quad (5.10)$$

where $f(\cdot)$ again is the transfer factor accounting for material effects upon the fluence. Equation (5.10) explicitly describes the dynamics of the temporal evolution of the pulse shape. Furthermore, equation (5.10) implies a differential relation on fluence, $d\Phi^{n+1} = f(\Phi^n) d\Phi^n$, which—after integrating over the limits $\Phi^n(-\infty) = 0$ and $\Phi^n(+\infty) = \Phi_{max}^n$ —produces a discrete *map on maximum fluence*:

$$\Phi_{max}^{n+1} = \int_0^{\Phi_{max}^n} f(\Phi') d\Phi' \equiv \mathcal{F}(\Phi_{max}^n). \quad (5.11)$$

For example, equation (5.4) is squared to give (to $\mathcal{O}(g^2, l^2, gl)$),

$$|\Psi|^2(t + \tau) = R^2 \left(1 + \frac{2g}{1 + aS_g(t)} - \frac{2l}{1 + bS_l(t)} \right) |\Psi|^2(t). \quad (5.12)$$

Introducing a round trip index n , we find from (5.11) for class B lasers ($\Phi^n(t) = \int_{-\infty}^t |\Psi^n|^2(t') dt'$),

$$\frac{d\Phi^{n+1}}{dt} = R^2 \left(1 + \frac{2g}{1 + a\Phi^n(t)} - \frac{2l}{1 + b\Phi^n(t)} \right) \frac{d\Phi^n}{dt} \quad (5.13)$$

$$= f(\Phi^n(t)) \frac{d\Phi^n}{dt}. \quad (5.14)$$

Iterating from initial data $\Phi^0(t)$, thereby produces

$$\begin{aligned} \frac{d\Phi^1}{dt} &= f(\Phi^0(t)) \frac{d\Phi^0}{dt}, \\ \frac{d\Phi^2}{dt} &= f(\Phi^1(t)) \frac{d\Phi^1}{dt} = f(\Phi^1(t)) f(\Phi^0(t)) \frac{d\Phi^0}{dt}, \\ &\vdots \\ \frac{d\Phi^{n+1}}{dt} &= \left(\prod_{i=0}^n f(\Phi^i(t)) \right) \frac{d\Phi^0}{dt}. \end{aligned} \quad (5.15)$$

By introducing the mapping function, $\mathcal{F}(\Phi) \equiv \int_0^\Phi f(\Phi') d\Phi'$, these results can be recast as,

$$\begin{aligned} \frac{d\Phi^1}{dt} &= \frac{d}{dt} \mathcal{F}(\Phi^0(t)), \\ \frac{d\Phi^2}{dt} &= \frac{d}{dt} \mathcal{F}(\Phi^1(t)) = \frac{d}{dt} \mathcal{F}(\mathcal{F}(\Phi^0(t))), \\ \frac{d\Phi^n}{dt} &= \frac{d}{dt} \mathcal{F}^n(\Phi^0(t)) = \frac{d}{dt} \mathcal{F}(\mathcal{F}(\mathcal{F}(\mathcal{F} \dots \mathcal{F}(\Phi^0(t))))). \end{aligned} \quad (5.16)$$

We interpret this result as follows: Starting with an arbitrary pulse shape, $|\Psi^0|^2(t)$, integrate to find $\Phi^0(t)$. Now, for each value of t , separately iterate $\mathcal{F}(\Phi^0(t))$ n -times giving the function of time $\mathcal{F}^n(\Phi^0(t))$. Differentiating over time t gives $d\Phi^n/dt = |\Psi^n|^2(t)$. We now consider the asymptotic behavior of $|\Psi^n|^2(t)$ (*i.e.*, as $n \rightarrow \infty$) for the three cases already sketched out in Figure (4.3), where we can view the figures as graphs of $\mathcal{F}(\Phi)$ *vs.* Φ . The three cases are as follows:

- A) Unstable origin: For any $\Phi > 0$, $\mathcal{F}^n(\Phi) \rightarrow \Phi_s$ as $n \rightarrow \infty$, where Φ_s is the unique stable fixed point $\mathcal{F}(\Phi_s) = \Phi_s$. Therefore, $\Phi^n(t)$ evolves to a step function with

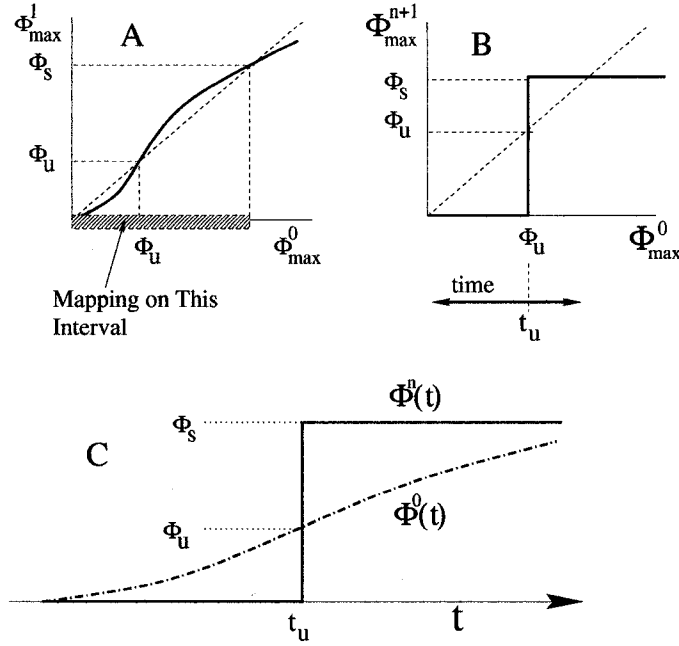


Figure 5.2: Delta collapse.

the step located at the *earliest time* when $|\Psi^0|^2(t)$ is non-zero. We note that if $\Phi^n(t)$ is a step, then $|\Psi^n|^2(t) = d\Phi^n/dt$ is δ -like. However, any spontaneous emission would contribute a non-zero value occurring at arbitrarily earlier times so that—even with a memory kernel of the form $K_{g,t}(t - t')$ —the pulse would be unstable to noise.

B) Stable behavior: Since $F(\Phi) < \Phi$ for all $\Phi > 0$, we have $\mathcal{F}^n(\Phi) \rightarrow 0$ as $n \rightarrow \infty$. Hence, any initial $\Phi^0(t)$ decays to zero.

C) Bistability: As we'll see, the bistable case combines the stable behavior of case B to suppress early perturbations, while amplifying signals which pass a finite threshold. For the bistable case, $\mathcal{F}^n(\Phi)$ vs. Φ asymptotically approaches the step function as outlined below and shown in Figure (5.2):

$$\lim_{n \rightarrow \infty} \mathcal{F}^n(\Phi) = \begin{cases} 0 & \text{when } 0 \leq \Phi < \Phi_u, \\ \Phi_u & \text{when } \Phi = \Phi_u, \\ \Phi_s & \text{when } \Phi_u < \Phi. \end{cases}$$

Since $\Phi^0(t)$ is monotonic in t , we need only compare $\Phi_{max}^0(t)$ to Φ_u . If $\Phi_{max}^0(t) < \Phi_u$, then $\Phi^n(t) \rightarrow 0$ as $n \rightarrow \infty$. If $\Phi_{max}^0(t) > \Phi_u$, then, since $\Phi^0(t)$ is monotonic, there is a unique time $t = t_u$ defined by $\Phi^0(t_u) = \Phi_u$. For $t < t_u$, $F^n(\Phi^0(t)) \rightarrow 0$; for $t > t_u$, $F^n(\Phi^0(t)) \rightarrow \Phi_s$. Hence, $\lim_{n \rightarrow \infty} \Phi^n(t) = \Phi_s H(t - t_u)$, where $H(\cdot)$ is the Heaviside function. The presence of noise—even if its effects are suppressed by bringing back the low-pass filters $S_{g,l} = \int_{-\infty}^t K_{g,l}(t - t') |\Psi^n|^2(t')$ —will tend to cause the point t_u to 'walk' toward progressively earlier times. This effect however, is much less dramatic than are the noise effects in case A. Therefore,

$$\frac{d}{dt} \lim_{n \rightarrow \infty} \frac{d}{dt} \Phi^n(t) = \Phi_s \delta(t - t_u) \quad (5.17)$$

CHAPTER 6

Memory Effects: Heuristic Approach

In this section we follow a heuristic approach in including memory effects by directly substituting the saturation integrals (containing the *slow* material response kernels) into the saturable gain and loss terms of equation (4.9):

$$\Psi(t + \tau) = R \left(1 + \frac{g}{1 + aS_l[|\Psi|^2](t)} - \frac{l}{1 + bS_g[|\Psi|^2](t)} \right) \Psi(t). \quad (6.1)$$

In optical models based on the Maxwell-Bloch equations for two-level atoms, it is found that the population inversion decrease exponentially with characteristic time scales, $\gamma_{g,l}^{-1}$ (recall that in Section 3, $\gamma_{g,l}^{-1}$ was defined to represent the homogeneous broadening terms for the gain and loss media, respectively [9]). Consequently we propose that we can write the response kernels as:

$$K_{g,l}(t, t') = K_{g,l}(t - t') = e^{-\gamma_{g,l}(t-t')}, \quad t \geq t'. \quad (6.2)$$

Inserting the fixed points of the train of constant power delta functions discussed above into the saturation integrals of equation (5.1), and performing the integration and the sum, produces the following, periodic saturation *functions*:

$$S_{g,l}(t) = \frac{|\Psi_*|^2 e^{\gamma_{g,l}(\lfloor \frac{t}{T} \rfloor T - t)}}{e^{\gamma_{g,l}T} - 1}. \quad (6.3)$$

In the above, $\lfloor \cdot \rfloor$ is the floor function and the new parameter space now consists of $\lambda \equiv \{R, g, l, a, b, \gamma_g, \gamma_l, T\}$. Consequently, setting $t = mT$, with m being an integer, and defining

$$\begin{aligned}
\tilde{a} &\equiv \frac{a}{e^{\gamma_g T} - 1}, \\
\tilde{b} &\equiv \frac{b}{e^{\gamma_l T} - 1}, \\
\tan \tilde{\theta} &\equiv \frac{\tilde{a}}{\tilde{b}};
\end{aligned} \tag{6.4}$$

the fixed point equation for this *additive map with memory* becomes:

$$\Psi_* = R \left(1 - \frac{l}{1 + \cos(\tilde{\theta})|\Psi_*|^2} + \frac{g}{1 + \sin(\tilde{\theta})|\Psi_*|^2} \right) \Psi_*; \tag{6.5}$$

The form of the above equation is identical to that of the fast map without memory defined by equation (4.9). This implies the global bifurcation scenarios found in the fast map are maintained; possibly with new ones occurring as well.

6.1 New Dynamical Behavior Associated with Memory Effects

In this section we consider the situation where the material relaxation times are on the order of the pulse round trip time but the pulse width is smaller by several orders of magnitude, *i.e.*, $\Delta t \ll \tau$. Such multiple scales are known to occur in optical systems when the nanosecond relaxation rates of the media are comparable to the cavity round-trip time and pulse widths are observed to be in the sub-picosecond range. This assumption of multiple-time scales allows us to reduce the infinite-dimensional system of (5.4) and (5.3) to a 5-dimensional map via singular perturbation theory or *two-timing*.

The two-timing approach allows a formal separation of the saturation integrals in (5.1) into two domains corresponding to whether a pulse is present (the inner region) or not (the outer). This situation is graphically illustrated in Figure (6.1) which is Figure (3.2) reproduced here for convenience. In the inner region, the integrals are dominated by the temporal scale of the pulse width—allowing neglect

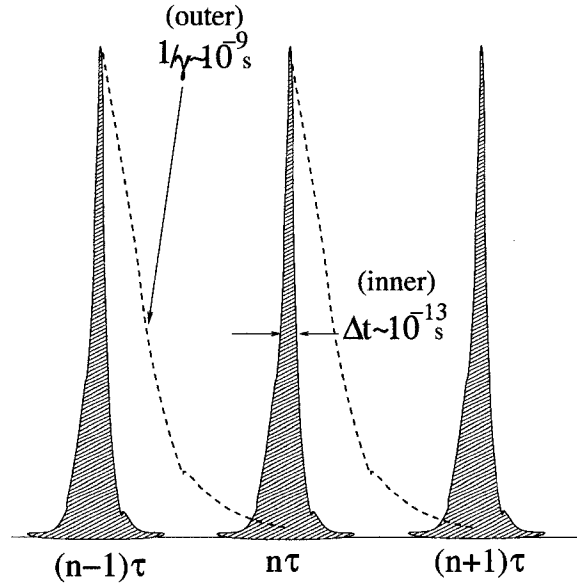


Figure 6.1: Inner and outer regions of the pulse train.

of the relaxation terms couched in the response kernels, $K_{g,t}(t, t')$. Integration over a pulse—while neglecting media response—thereby produces the maximum fluence Φ_{max} defined by equation (5.9). As depicted in Figure (6.1), the outer region is dominated by the temporal scales associated with residual effects within the media as a result of the previous pulse. Formally evaluating the saturation integrals over these two time scales therefore produces the following scheme:

$$S_g(t) = \Phi_{max}(t) + \alpha S_g(\text{previous pulses}) \quad (6.6)$$

$$S_l(t) = \Phi_{max}(t) + \beta S_l(\text{previous pulses}) \quad (6.7)$$

where, $\alpha \equiv e^{-\gamma\tau}$ and $\beta \equiv e^{-\gamma\tau}$. These expressions suggest a new map on intensity in which the maximum fluence function and saturation integrals are the new state variables—coupled through a new multivariate transfer factor:

$$f(\Phi_{max} + \alpha S_g, \Phi_{max} + \beta S_l) =$$

$$R^2 \left(1 + \frac{2g}{1 + a(\Phi_{max} + \alpha S_g)} - \frac{2l}{1 + b(\Phi_{max} + \beta S_l)} \right). \quad (6.8)$$

Integration of equation (6.8) therefore produces a multivariate function of the fluence and saturation integrals, $\mathcal{F}(\cdot, \cdot, \cdot)$:

$$\mathcal{F}(\Phi_{max} + \alpha S_g, \Phi_{max} + \beta S_l) \equiv \int_0^{\Phi_{max}} f(\Phi' + \alpha S_g, \Phi' + \beta S_l) d\Phi'. \quad (6.9)$$

Equations (6.6)-(6.9) form a system that couples the present $(n+1)^{th}$ time step to the preceding n^{th} and $(n-1)^{th}$ time steps (see Figure (6.1)). The memory of the gain is accounted for by α and that of the absorber by β . These equations, and the scheme outlined by (6.6) and (6.7), result in a low dimensional dynamical system now composed of maps on the saturation integrals and the fluence:

$$\begin{aligned} S_g^{n+1} &= \Phi_{max}^n + \alpha S_g^{n-1}, \\ S_l^{n+1} &= \Phi_{max}^n + \beta S_l^{n-1}, \\ \Phi_{max}^{n+1} &= \mathcal{F}(\Phi_{max}^n + \alpha S_g^{n-1}, \Phi + \beta S_l^{n-1}); \end{aligned} \quad (6.10)$$

To facilitate analysis of (6.10), we introduce the following scales and change of notation: $\theta = b/a$, $x_1^n = aS_g^n$, $x_2^n = bS_l^n$, $x_3^n = b\Phi_{max}^n$, $x_4^n = aS_g^{n-1}$, $x_5^n = aS_l^{n-1}$. With these definitions, we see that $x \in \mathbb{R}^5$, and equations (6.9) and (6.10) become:

$$\begin{aligned} x_1^{n+1} &= \frac{x_3^n}{\theta} + \alpha x_4^n, \\ x_2^{n+1} &= x_3^n + \beta x_5^n, \\ x_3^{n+1} &= h(x_1^n, x_2^n, x_3^n), \\ x_4^{n+1} &= x_1^n, \\ x_5^{n+1} &= x_2^n, \end{aligned} \quad (6.11)$$

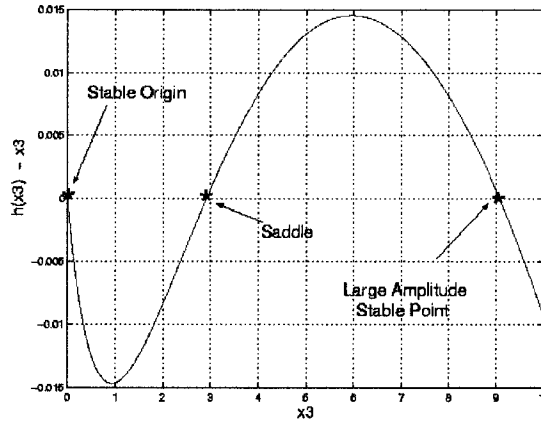


Figure 6.2: Plot of (6.13) under bistable conditions.

where the integration of the transfer factor (6.8) produces a transcendental function in $\{x_3^n, x_4^n, x_5^n\}$, defined as

$$h(x_1^n, x_2^n, x_3^n) = R^2 \left(x_3^n + 2g\theta \ln \left(1 + \frac{x_3^n}{\theta(1 + \alpha x_4^n)} \right) - 2l \ln \left(1 + \frac{x_3^n}{(1 + \beta x_5^n)} \right) \right). \quad (6.12)$$

6.2 Stability Analysis

In this section, we perform a stability analysis of the dynamical system (6.11). Determination of the fixed points of this system, \bar{x}_i , is reduced to numerically (or graphically) determining the roots of $h(\bar{x}_3) - \bar{x}_3$, since in steady-state, $h(\bar{x}_3, \bar{x}_4, \bar{x}_5) \rightarrow h(\bar{x}_3)$; explicitly, the transcendental equation to solve is

$$(R^2 - 1) \bar{x}_3 + R^2 2g\theta \ln \left(1 + \frac{\bar{x}_3}{\theta + \frac{\alpha \bar{x}_3}{1 - \alpha}} \right) - R^2 2l \ln \left(1 + \frac{\bar{x}_3}{1 + \frac{\beta \bar{x}_3}{1 - \beta}} \right) = 0. \quad (6.13)$$

Figure (6.2) is a plot of equation (6.13) for parameter values that exhibit bistability.

In a region of parameter space that is consistent with a fast absorber with ($\beta \ll$

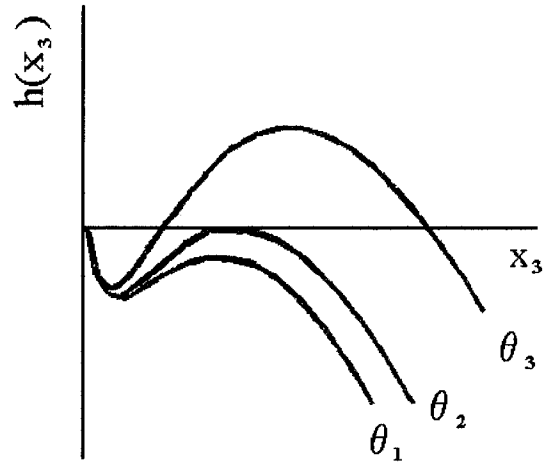


Figure 6.3: 5d Saddle-Node.

1), the 5-dimensional system was found to also exhibit a saddle-node bifurcation as shown in Figure (6.3), where the parameter θ is varied for fixed $\{R, g, l, T, \gamma_g, \gamma_l\}$. In addition, an exchange of stability at threshold, analogous to the pitch-fork bifurcation in the fast map was found to occur as well (not shown).

Linearizing about the fixed points of (6.11) results in the following Jacobian matrix whose eigenvalues $\{\zeta_i\}$ characterize the spectrum

$$J(\bar{x}) = \begin{bmatrix} 0 & 0 & \frac{1}{\theta} & \alpha & 0 \\ 0 & 0 & 1 & 0 & \beta \\ 0 & 0 & \Sigma & g\Gamma & l\Lambda \\ 1 & 0 & 0 & 0 & 0 \\ 0 & 1 & 0 & 0 & 0 \end{bmatrix}; \quad (6.14)$$

where,

$$\Sigma(\bar{x}_3; \lambda) = R^2 \left(1 + 2 \frac{g}{1 - \frac{\bar{x}_3}{\theta(\alpha-1)}} - 2 \frac{l}{1 - \frac{\bar{x}_3}{\beta-1}} \right) \quad (6.15)$$

$$\Gamma(\bar{x}_3; \lambda) = -\alpha\theta \frac{2\bar{x}_3 R^2}{\left(\theta - \frac{\alpha\bar{x}_3}{\alpha-1}\right) \left(1 - \frac{\bar{x}_3}{\theta(\alpha-1)}\right)} \quad (6.16)$$

$$\Lambda(\bar{x}_3; \lambda) = \beta \frac{2\bar{x}_3 R^2}{\left(1 - \frac{\beta\bar{x}_3}{\beta-1}\right) \left(1 - \frac{\bar{x}_3}{\beta-1}\right)}. \quad (6.17)$$

The characteristic polynomial, whose roots are the eigenvalues, is thus a quintic function of the form

$$\begin{aligned} \det(J - \lambda\mathbb{I}) &\equiv P(\zeta) & (6.18) \\ &= \zeta^5 - \Sigma\zeta^4 - (\beta + \alpha)\zeta^3 \\ &\quad + (\alpha(\Sigma - g\Gamma) + \beta(\Sigma - l\Lambda))\zeta^2 + \alpha\beta\zeta \\ &\quad + \beta\alpha(g\Gamma + l\Lambda - \Sigma); \end{aligned}$$

where \mathbb{I} is the 5x5 identity matrix.

Given that both g and l are on the order of a few percent for a single pass, we adopt a perturbative approach in solving (6.18) by first setting terms involving these factors to zero. As depicted in Figure (6.4), these limits result in a set of real valued eigenvalues $\{\pm\sqrt{\alpha}, \pm\sqrt{\beta}, \Sigma\}$. Note that, in these limits, only Σ depends upon which fixed point the Jacobian is evaluated at; hence, under bistable conditions, we let $\Sigma = \Sigma_s$ for the large amplitude stable point, $\Sigma = \Sigma_o$ for the stable origin and the $\Sigma = \Sigma_u$ for the unstable saddle. Accordingly, Σ_s is shown in Figure (6.4) to be inside the unit circle as would Σ_o (not shown in the figure); Σ_u (also not shown) would lie just outside the unit circle. For the fixed point at the origin, $\bar{x}_3 \rightarrow 0 \Rightarrow \Sigma \rightarrow R^2(1 + 2g - 2l)$ which defines the gain cap, and Γ and $\Lambda \rightarrow 0$. In the limits $g, l \rightarrow 0$, $\Sigma_{s,o,u} \rightarrow R^2 < 1$ and all terms in Γ and $\Lambda \rightarrow 0$ as well.

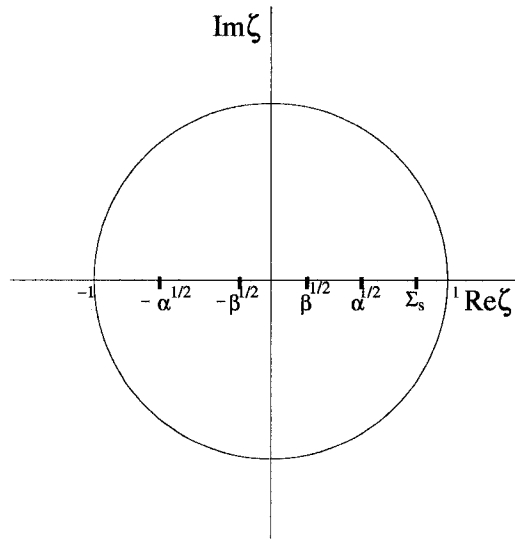


Figure 6.4: Perturbative spectra.

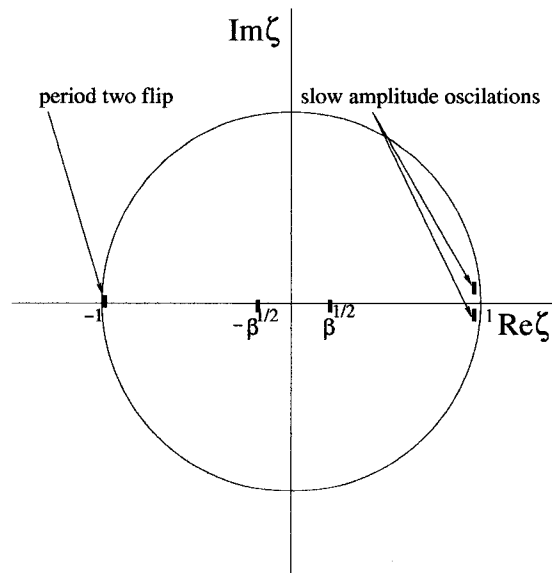


Figure 6.5: Spectra showing period two flip orbits and breathing oscillations.

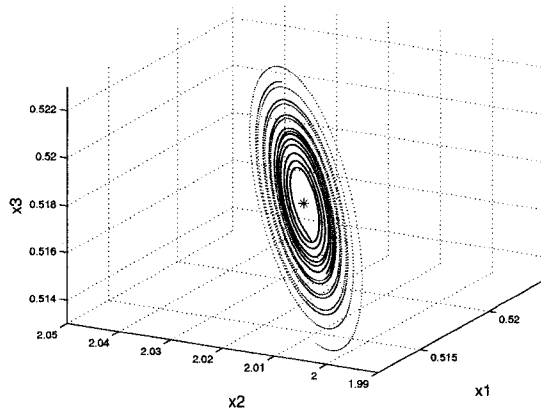


Figure 6.6: Phase space after the occurrence of the Hopf bifurcation.

An important consequence of the above analysis, depicted in Figure (6.5), arises in the degenerate situation where $\sqrt{\alpha} \rightarrow \Sigma_s \leq 1$. In this limit, the root $-\sqrt{\alpha}$ is seen to represent a weakly damped period-two oscillation (a *flip*), and the degeneracy of $\sqrt{\alpha} \sim \Sigma_s$ implies the possibility that, when g and l are reintroduced as perturbations, the roots can form a conjugate pair—signifying the existence of slowly damped oscillatory behavior. For the degenerate case where $\sqrt{\alpha} \rightarrow \Sigma_u \geq 1$, the systems undergoes a bifurcation (Hopf) that results in unstable oscillations. Figure (6.6) reveals the phase space of the system under these conditions for a parameter set $\{g, l, \theta\} = \{0.084, 0.061, 80.0\}$ but with $\alpha \simeq 0.954$ which corresponds to a gain relaxation rate that was increased in magnitude from a value of $\gamma_g = 0.25$ (used in all previous runs) to $\gamma_g = 0.38$. (Recall, $\alpha \equiv e^{-\gamma_g \tau}$ and therefore an increase in magnitude or α corresponds to a increase in memory effects.) The unstable oscillations of the fluence variable are shown in Figure (6.7) for a set of three different initial conditions chosen at random around the unstable node. We interpret these oscillatory modes to indicate the existence of *breather modes* in the integrated intensity or fluence variables.

We now turn our attention to the central prediction of the slow map containing

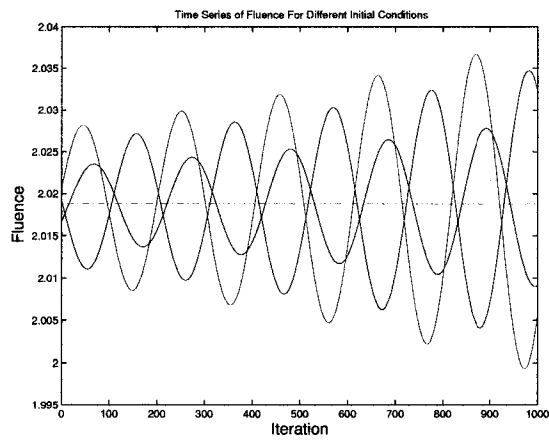


Figure 6.7: Time series revealing unstable oscillations after the Hopf bifurcation.

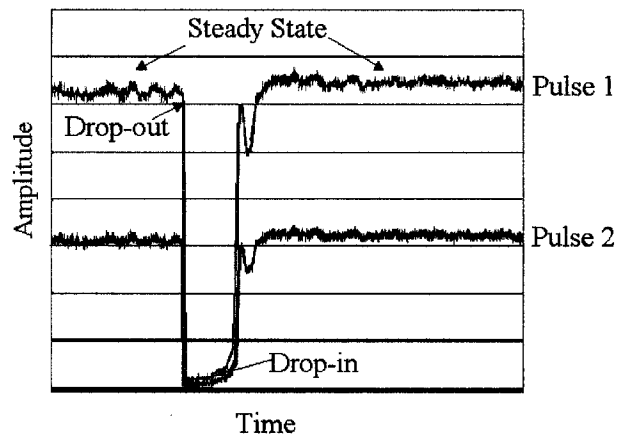


Figure 6.8: Experimental time series showing drop-out and drop-in data in arbitrary amplitude units for two, counter-propagating pulses.

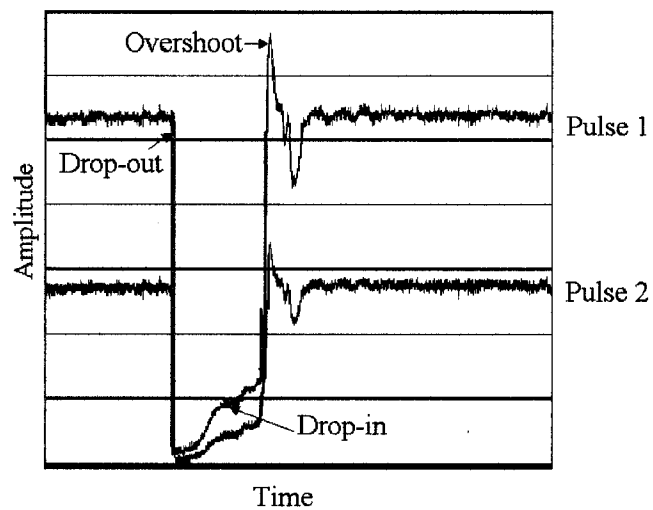


Figure 6.9: Experimental time series showing drop-out, drop-in and overshoot phenomena.

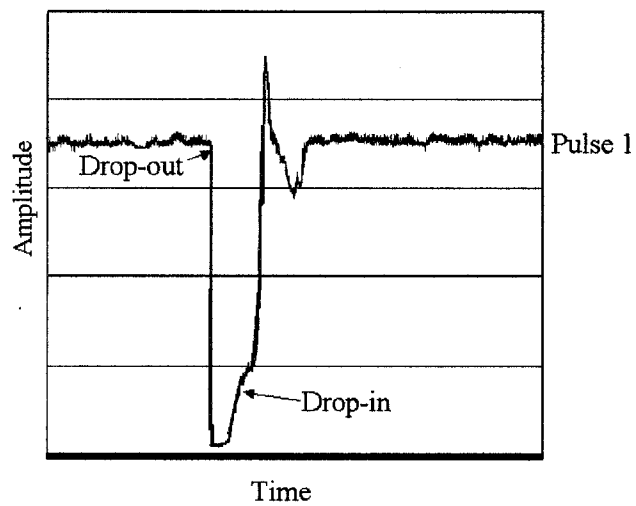


Figure 6.10: Experimental time series for a single, uni-directional pulse.

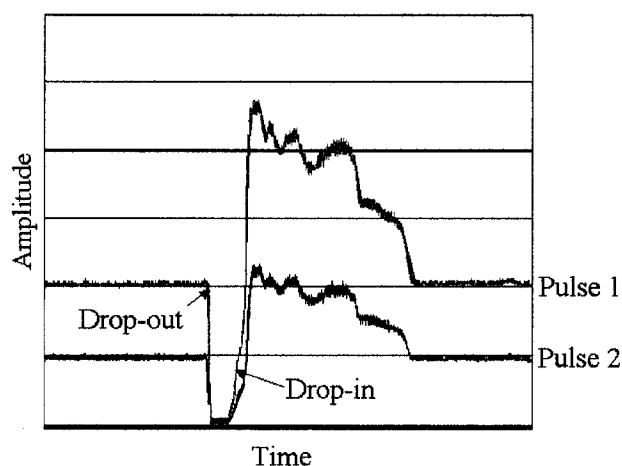


Figure 6.11: Experimental time series.

memory: the existence of a type of hysteresis in the dynamical behavior of drop-out and drop-in events. Figures (6.8) to (6.13) are experimental time series of drop-out and drop-in events for different values of the pump gain as observed in the CPM laser at William & Mary. These data sets will be fully discussed in Wie Yang's Ph.D. dissertation in the near future [17]. It is worthy of note that the experimental undertaking that produced these graphs was initiated as a direct consequence of our model's prediction of this asymmetry. The plots depict variations in pulse amplitude over time (temporal units are 10ns) for both single pulse situations and for the case involving two counter propagating pulses denoted as *pulse 1* and *pulse 2* where applicable. Figure (6.10) shows a single, uni-directional pulse case. These plots attest to the rich variety of dynamics associated with pulse formation and cessation. Particular features to note include the substantial differences in the time over which drop-outs occur as compared to the times associated with drop-ins. Also note the occurrence of *overshoot* where there is a large spike in amplitude followed by a decrease in output as the pulse settles back to a steady state. In Figure

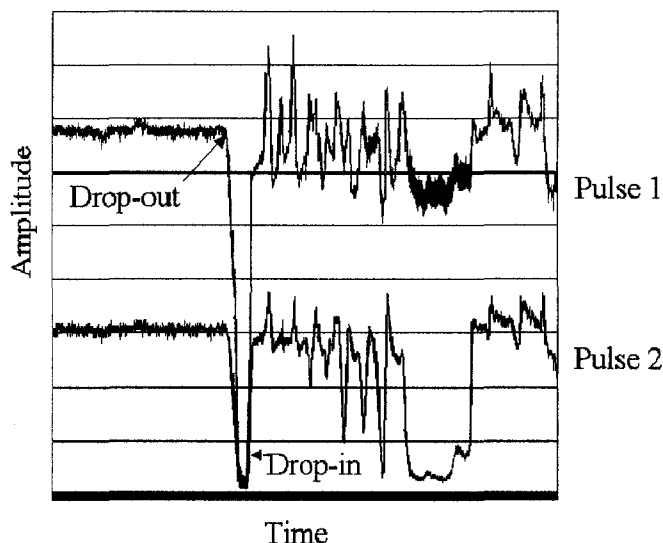


Figure 6.12: Experimental time series showing chaotic-like instability.

(6.11) there is an unusually long time after a drop-in event over which the system relaxes back to its former lasing state. Figure (6.12) is particularly interesting in its *chaotic-like attempt* to stabilize after a drop-out had occurred. Finally, as seen most clearly in Figure (6.13), the steady-state after a drop-out-drop-in sequence can possess a greater average amplitude as compared to the average amplitude prior to drop-out; also note in Figure (6.13) that drop-in rates can even differ between counter-propagating pulses that exist simultaneously in the cavity as well.

The model's prediction of this asymmetric behavior between the drop-out and drop-in events follows from an analysis of the phase space of the slow map (6.11). In particular, we show that for a critical parameter set under bistable conditions, the topological structure of the stable and unstable manifolds embedded in the phase space have their respective basin boundaries in close proximity to each other. As a consequence, it is postulated that the system can experience dramatic state changes via *noise-induced hopping* between the basin of the stable origin and the basin of

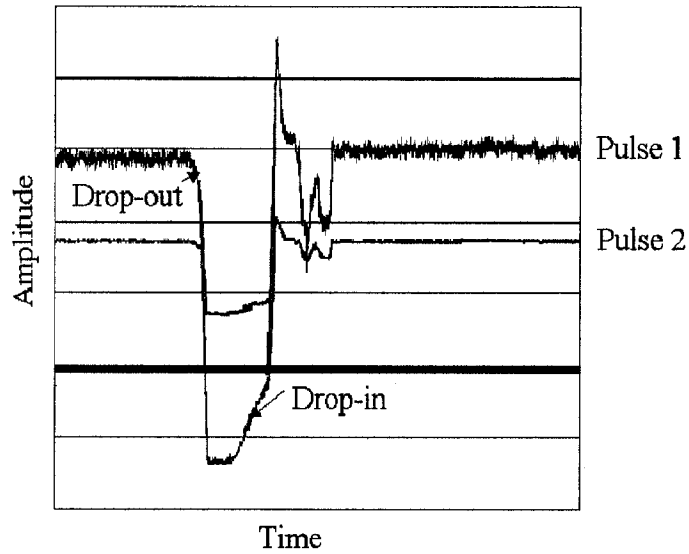


Figure 6.13: Experimental time series showing asymmetry between counter-propagating pulses.

the stable node. Figure (6.14) notionally illustrates these phenomenon for a three dimensional system discussed next.

To aid in the analysis and visualization of the stable and unstable manifolds for the full 5-dimensional system, we simplify by setting the saturation parameter for the absorber $\beta = 0$. This simplification reduces the 5-dimensional system to the following 3-dimensional *reduced map*

$$\begin{aligned}
 x_1^{n+1} &= \frac{x_2^n}{\theta} + \alpha x_3^n, \\
 x_2^{n+1} &= R^2 \left(x_2^n + 2g\theta \ln \left(1 + \frac{x_2^n}{\theta(1 + \alpha x_3^n)} \right) - 2l \ln(1 + x_2^n) \right), \\
 x_3^{n+1} &= x_1^n.
 \end{aligned} \tag{6.19}$$

Thus, with this simplification, the full 5-dimensional system can be thought of as a perturbed version of this 3-dimensional one where memory effects in the absorber are ignored.

The Jacobian associated with (6.19) is

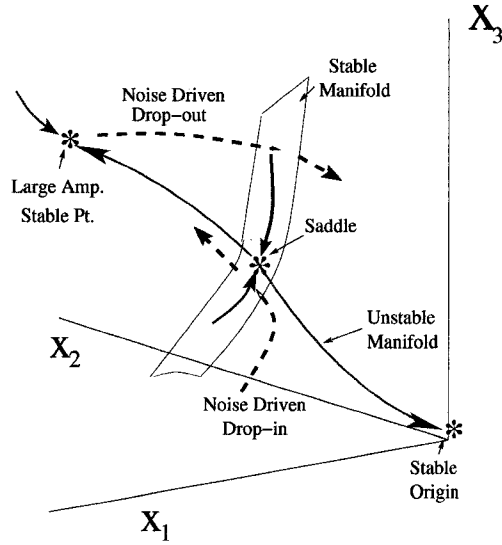


Figure 6.14: Suggestive phase portrait for linearized system with $\beta = 0$ depicting hysteresis in drop-out and drop-in phenomena.

$$J = \begin{bmatrix} 0 & \frac{1}{\theta} & \alpha \\ 0 & j_{22}(x_2, x_3; \lambda) & j_{23}(x_2, x_3; \lambda) \\ 1 & 0 & 0 \end{bmatrix}, \quad (6.20)$$

where

$$j_{22}(x_2, x_3; \lambda) \equiv R^2 \left(1 + \frac{2g}{1 + \frac{x_2}{\theta} + \alpha x_3} - \frac{2l}{1 + x_2} \right), \quad (6.21)$$

$$j_{23}(x_2, x_3; \lambda) \equiv -\frac{2R^2 g \alpha x_2}{\left(1 + \frac{x_2}{\theta} + \alpha x_3\right) (1 + \alpha x_3)}. \quad (6.22)$$

In the limiting case examined above where $g, l \rightarrow 0$, the Jacobian becomes

$$J = \begin{bmatrix} 0 & \frac{1}{\theta} & \alpha \\ 0 & R^2 & 0 \\ 1 & 0 & 0 \end{bmatrix}, \quad (6.23)$$

which, when transformed into its diagonal form gives

$$Diag(J) = \begin{bmatrix} R^2 & 0 & 0 \\ 0 & \sqrt{\alpha} & 0 \\ 0 & 0 & -\sqrt{\alpha} \end{bmatrix}. \quad (6.24)$$

Thus, the eigenvalues of J in this limit are seen to be $\{R^2, \sqrt{\alpha}, -\sqrt{\alpha}\}$ and the eigenvectors are found to be

$$\begin{aligned} v_1(R^2) &= (R^2, \theta(R^4 - \alpha), 1), \\ v_2(\sqrt{\alpha}) &= (\sqrt{\alpha}, 0, 1), \\ v_3(-\sqrt{\alpha}) &= (-\sqrt{\alpha}, 0, 1). \end{aligned} \quad (6.25)$$

Notice that when $R^2 = \sqrt{\alpha}$, the eigenvectors v_1 and v_2 become degenerate. When this occurs, the Jacobian matrix will not be diagonalizable and what is called a *Takens-Bogdanov* bifurcation occurs. Accordingly, under these conditions, the non-linear response to perturbations is expected to be very different than for systems that are diagonalizable [18, 19]. Detailed analysis of these scenarios and the associated dynamical ramifications for the CPM laser are presently in progress.

Figure (6.15) displays trajectories in the phase space that exhibit the period-two fast oscillations (*flip orbits*) discussed above for five different sets of initial conditions that lie on the basin of attraction for the unstable manifold. Each initial condition is delineated in the figure by a separate color and the location of the saddle-node for this parameter set is shown as a red asterisk. At the time of this writing, this high frequency oscillation has not yet been unambiguously detected in the CPM laser at William & Mary. For clarity in the following graphs, we henceforth only display every other point along a trajectory in the phase-space to remove the period-two flip orbit. Figure (6.16) was generated under the same conditions as Figure (6.15)

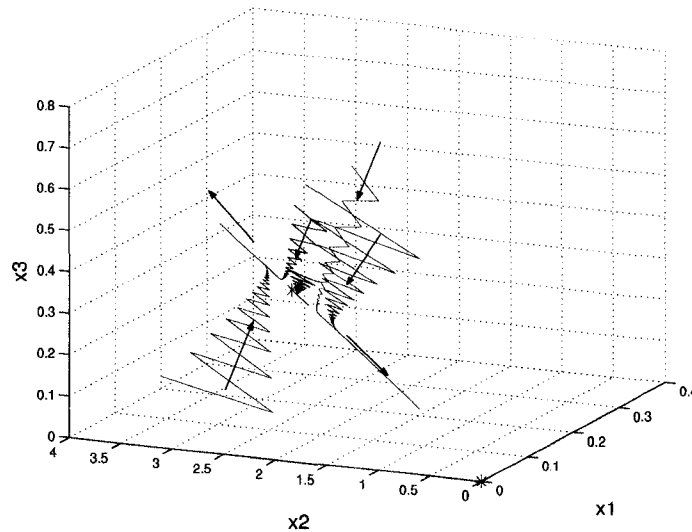


Figure 6.15: Phase portrait around saddle showing period-two oscillations.

and shows the effects of this strategy.

Figures (6.17) and (6.18) display samplings of the saddle's stable manifold in blue and the unstable manifold in red for the positive quadrant of the phase space. As in the notional graph of Figure (6.14), the large amplitude stable fixed point and the stable origin are marked by blue asterisks and the saddle point is indicated by a red asterisk. The figures reveal different orientations of the manifolds formed from a set of 700 initial conditions for the stable manifold and 10 for the unstable. These initial conditions are chosen in a pseudo-random manner from a normally distributed *epsilon-ball* of values centered around the saddle node (see Section 8.2 in the Appendix for further discussion on the technique used to sample the stable manifold as well as generate the initial conditions). Figure (6.19) is a cartoon of the immediate neighborhood surrounding the intersection of the manifolds drawn to illustrate the non-transverse nature of the intersection (see [20, 16]), *i.e.*, the *cusplike* topology surrounding the unstable saddle. This cartoon is based upon many numerical results involving various configurations of initial conditions and is

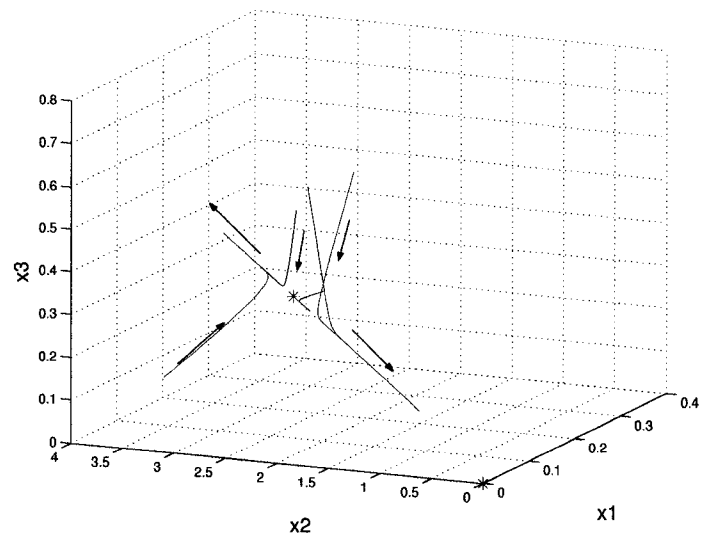


Figure 6.16: Same trajectories as Figure (6.15) but with period-two oscillations removed.

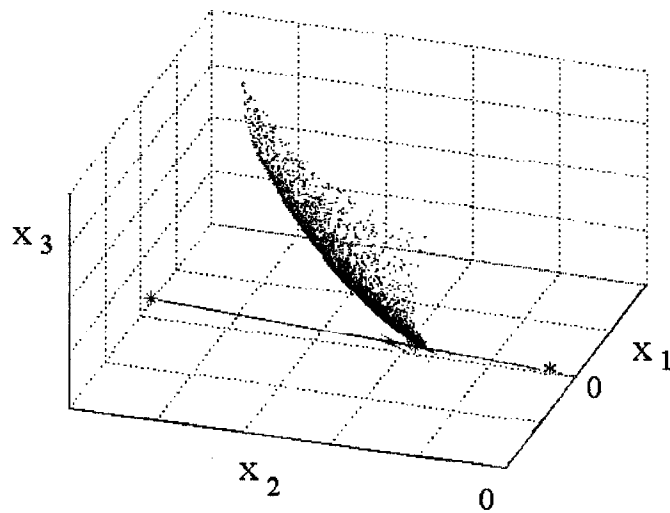


Figure 6.17: Numerical phase portrait for reduced system (6.19) under bistable conditions.

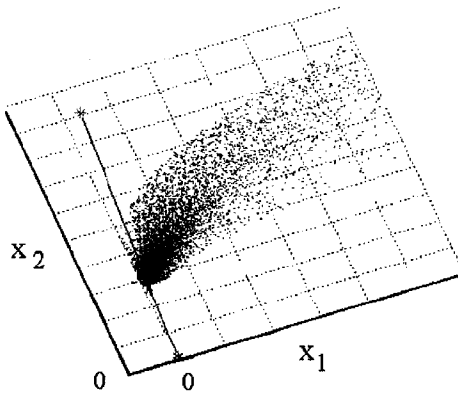


Figure 6.18: Rotated view of Figure (6.17).

exemplified by Figure (6.20). In Figure (6.20), the green asterisk marks the location of the saddle.

Figure (6.21) displays a set of time series for the fluence variable in the 3-dimensional reduced system. Each color in the plot represents a different initial condition randomly chosen from the surrounding neighborhood of the saddle. Also displayed in the figure are the large amplitude stable point and the unstable saddle. As the figure shows, all of the trajectories approach the stable points monotonically. Figure (6.22) shows time series plots for the saturation integral of the reduced system. For this variable, the initial conditions were such that the trajectories flow initially towards the unstable saddle before wandering off to the stable points. Figures (6.23) and (6.24) reveal the phase space and time series just before the saddle-node bifurcation occurs, respectively. In Figure (6.23), the near degeneracy of the fixed points and the reduced transversality of the manifolds (cusp-like topology of the stable manifold) are evident.

To explore the trans-critical bifurcation in the reduced system, the value for the gain parameter was increased to a value just before the stable origin and the

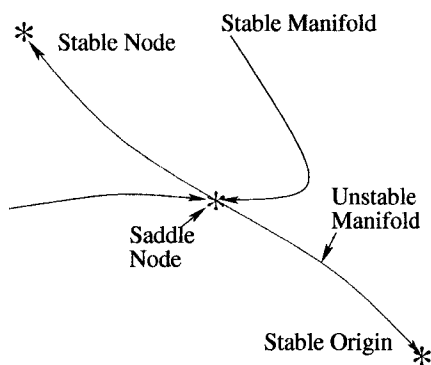


Figure 6.19: Cartoon of manifold intersection.

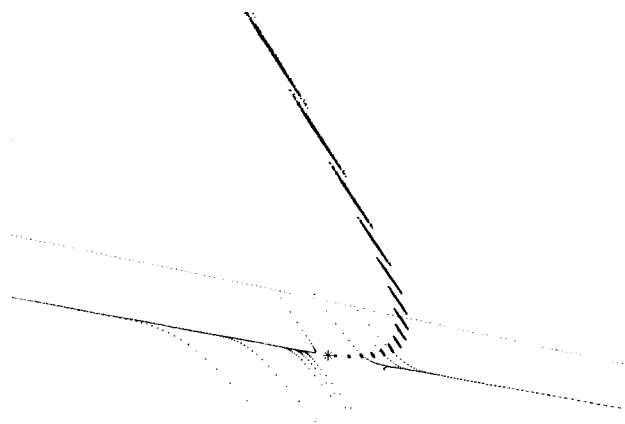


Figure 6.20: Magnified view of numerical sampling around manifold intersection.

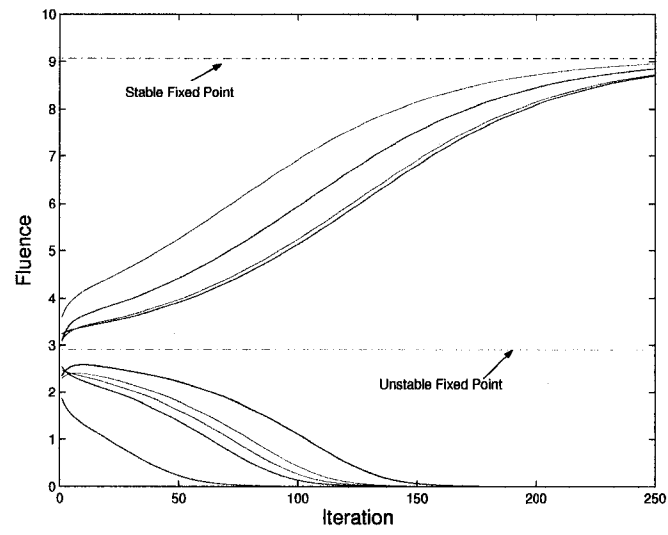


Figure 6.21: Time series (6.19) for fluence.

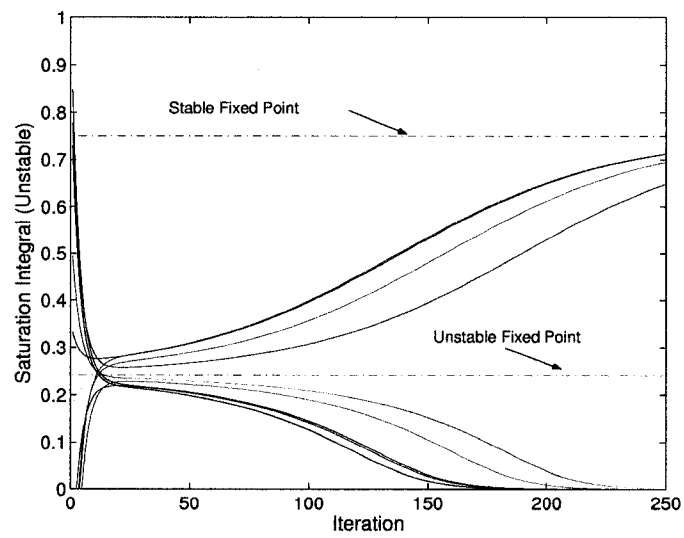


Figure 6.22: Time series (6.19) for saturation integral.

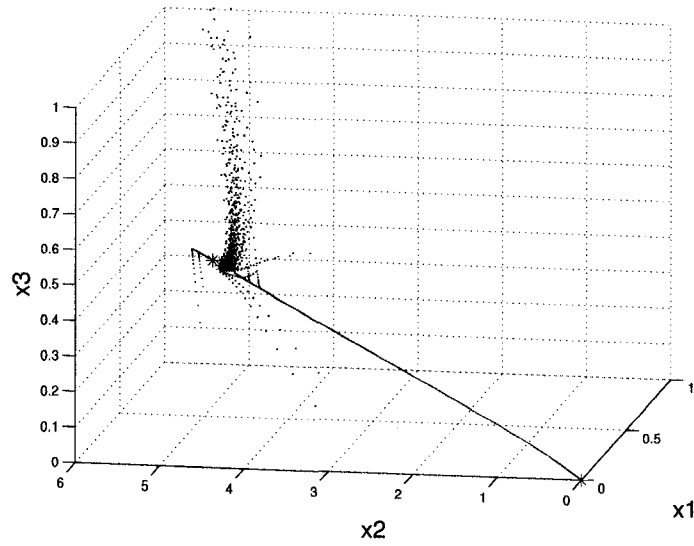


Figure 6.23: Phase portrait just before saddle-node bifurcation.

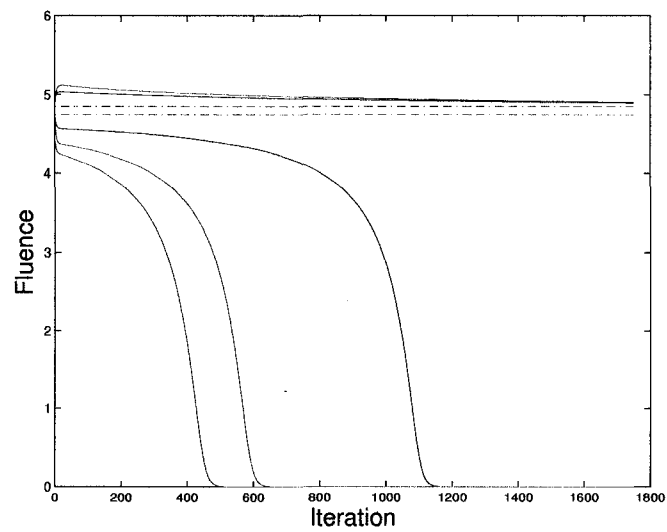


Figure 6.24: Time series just before saddle-node bifurcation.

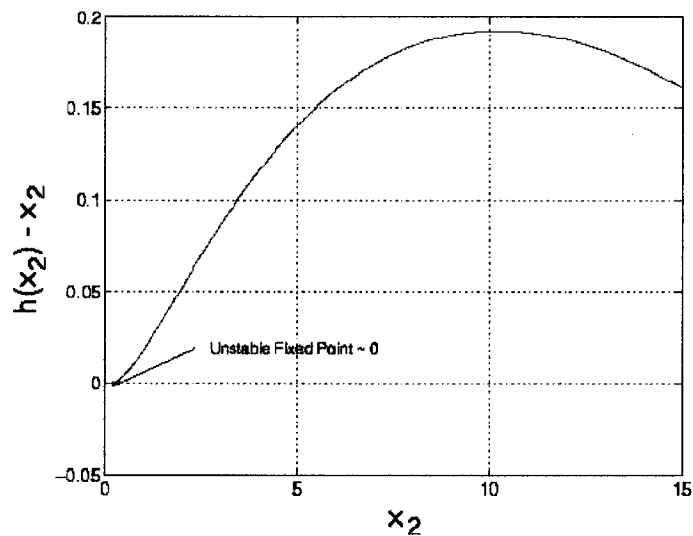


Figure 6.25: Trans-critical bifurcation fixed point equation.

unstable saddle become degenerate. The transcendental function to determine the fixed point \bar{x}_2 is shown in Figure (6.25) under these conditions. Figure (6.26) and (6.27) reveal different views of the stable and unstable manifolds where the increase in transversality as compared to the bistable case is evident.

In summary, it has been shown that under bistable conditions, the topological structure of the manifolds exhibits a diminished transversality of intersection between the stable and unstable manifolds. Accordingly, it is postulated that—with the addition of noise—the state trajectories associated with drop-outs proceed along very different paths in the phase space as compared to those representing pulse formation or drop-ins. This asymmetry in dynamics is the primary prediction of the models presented in this thesis.

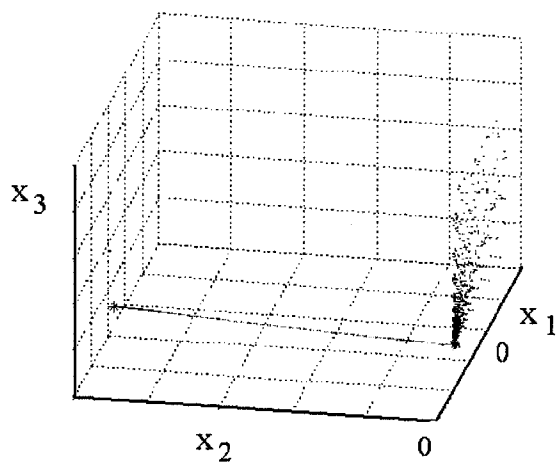


Figure 6.26: Phase space just before trans-critical bifurcation.

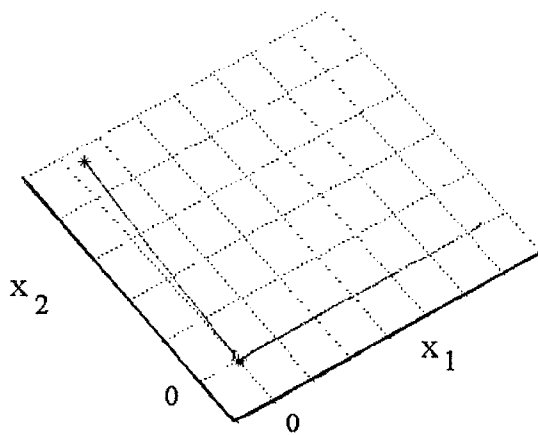


Figure 6.27: Rotated view of Figure (6.26).

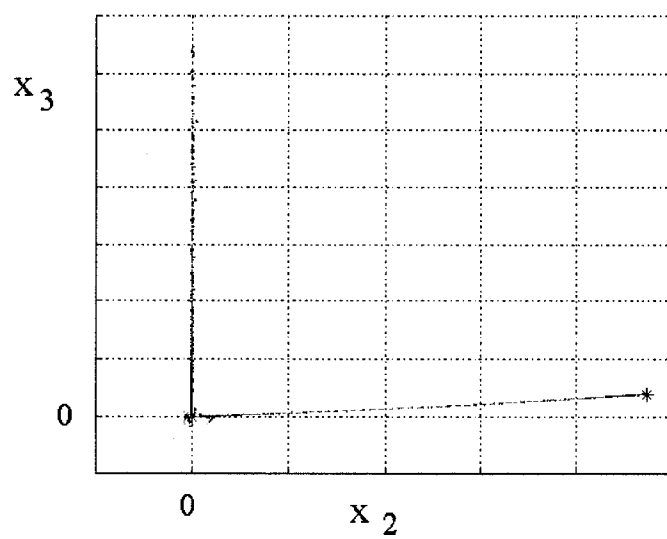


Figure 6.28: Third view of Figure (6.26).

CHAPTER 7

Conclusions

In this dissertation, we have developed phenomenological models to aid in understanding the spontaneous formation of pulses and their subsequent dynamics for systems in which there exists regions of saturable gain and absorption—as typified in colliding pulse mode-locked dye lasers. In particular, we modeled unidirectional pulse formation and stability in systems exhibiting bistability and feedback leading to memory effects. Key results of this work are as follows:

1. Improved understanding of the interplay between bistability and spontaneous pulse formation in slow media;
2. A new method for incorporating pulse-to-pulse memory effects, leading to the development of low-dimensional maps incorporating the effect;
3. The discovery of highly degenerate bifurcations in these maps that suggest a large difference between drop-out and drop-in dynamics, which has since been observed;
4. Model based prediction of breather modes yet to be observed.

Future extensions of this research could include incorporation of dispersion, finite gain bandwidth, and the Kerr effect; all of which contribute to the pulse shape. Noise effects should also be considered.

CHAPTER 8

Appendix

8.1 Light and Matter

In this section, we derive from first principles the *raw Maxwell–Bloch* equations. These equations model the interaction of light and matter and result from the coupling of the time dependent Schrödinger equation with the field equations of Maxwell. Treatment of the radiation field as a classical observable is justified by the large photon flux densities present in the types of optical systems we consider here (see [1]).

We begin with the time dependent Schrödinger Equation,

$$i\hbar\partial_t\Phi(\mathbf{r},t) = \hat{H}(\mathbf{r})\Phi(\mathbf{r},t); \quad (8.1)$$

where $\hat{H}(\mathbf{r})$ denotes the spatially dependent Hamiltonian and $\Phi(\mathbf{r},t)$ represents the state eigenfunction describing the atomic system for a single atom. Adopting a perturbative approach, we define the perturbative Hamiltonian

$$\hat{H}(\mathbf{r}) \equiv \hat{H}_o + \delta\hat{U}(\mathbf{r}), \quad (8.2)$$

with $\delta\hat{U}(\mathbf{r})$ describing the perturbed potential energy operator. For electronic transitions, the unperturbed Hamiltonian \hat{H}_o contains a Coulomb interaction term $(-kq^2/r)$, where k is the Coulomb constant and r is the distance from the nucleus. Thus, \hat{H}_o satisfies

$$\hat{H}_o\phi_i = \hbar\omega_i\phi_i; \quad (8.3)$$

where the $\{\phi_i\}$ form a complete orthonormal basis satisfying $\int d^3\mathbf{r}\phi_i^*\phi_j = \delta_{i,j}$. In the presence of an electric field $\mathbf{E}(\mathbf{r}, t)$, the perturbed Hamiltonian is derived from the classical identity

$$\Delta\hat{U} = q\Delta\hat{V} = q \int \mathbf{E} \cdot d\mathbf{r}. \quad (8.4)$$

Since the field is approximately constant over atomic scale, we can take $\mathbf{E}(\mathbf{r}, t) \approx \mathbf{E}(t)$. Under this approximation, the perturbation potential becomes

$$\delta\hat{U} \simeq -q\mathbf{E} \cdot \mathbf{r}. \quad (8.5)$$

Given $\{\phi_i\}$, the linearity of (8.1) implies that the general solution for a single atom is of the form

$$\psi(\mathbf{r}, t) = \sum a_j(t)\phi_j(\mathbf{r}). \quad (8.6)$$

In (8.6), $a_j(t)$ denotes the time-dependent complex probability amplitude associated with the occupation of the j th atomic state. Note that if $\hat{H} = \hat{H}_o$, then $a_j(t) = a_j(0)\exp(i\omega_j t)$.

For an ensemble of N identical atoms indexed by α , (8.6) becomes

$$\psi^\alpha(\mathbf{r}, t) = \sum a_j^\alpha(t)\phi_j(\mathbf{r}). \quad (8.7)$$

Introducing the *density matrix* of quantum statistical mechanics, defined by its matrix elements

$$\rho_{mm}(t) \equiv \frac{1}{N} \sum_{\alpha} (a_n^\alpha(t))^* a_m^\alpha(t), \quad (8.8)$$

the ensemble average associated with a physical observable A is calculated in the usual way; *i.e.*

$$\langle A \rangle = \text{Tr}(\rho A) \quad (8.9)$$

$$\begin{aligned} &= \sum \rho_{mn} A_{nm} \\ &= \frac{1}{N} \sum_{\alpha} \sum (a_n^{\alpha})^* a_m^{\alpha} \int \phi_n^* A \phi_m d^3 \mathbf{r}, \end{aligned} \quad (8.10)$$

where, $A_{nm} \equiv \int \phi_n^* A \phi_m d^3 r$. For laser cavities consisting of coherent photons, the probability amplitudes defined by equation (8.6) characterize *pure states*; implying that the only non-zero terms in (8.8) lie along the diagonal. Combining (8.1) through (8.8) results in a master equation governing the population dynamics of the many-body system:

$$i\hbar \sum \partial_t a_j(t) \phi_j(\mathbf{r}) = \sum a_j(t) \omega_j \hbar \phi_j(\mathbf{r}) - q \mathbf{E}(t) \cdot \mathbf{r} \sum a_j(t) \phi_j(\mathbf{r}). \quad (8.11)$$

From (8.11) we can now derive the *raw Maxwell-Bloch equations* that describe the dynamics of the occupation probabilities encoded by elements of the density matrix (8.8). Denoting the *dipole transition matrix* as

$$\mathbf{p}_{kl} \equiv q \int \phi_k^*(\mathbf{r}) \mathbf{r} \phi_l(\mathbf{r}) d\mathbf{r}, \quad (8.12)$$

we multiply (8.11) through by $\phi_k^*(\mathbf{r})$ and integrate over the spatial variable \mathbf{r} to arrive at

$$\partial_t a_k(t) = -i\omega_k a_k(t) + \frac{i}{\hbar} \mathbf{E}(t) \cdot \sum a_l(t) \mathbf{p}_{kl}, \quad (8.13)$$

and its complex conjugate

$$\partial_t a_k^*(t) = i\omega_k a_k^*(t) - \frac{i}{\hbar} \mathbf{E}(t) \cdot \sum a_l^*(t) \mathbf{p}_{kl}. \quad (8.14)$$

(Note that \mathbf{p} is Hermitian, *i.e.* $\mathbf{p}_{kl} = \mathbf{p}_{lk}^*$.) To cast the problem in terms of the density matrix, we invoke the identity $\partial_t \rho_{jk}(t) = \partial_t a_j(t) a_k^*(t) + a_j(t) \partial_t a_k^*(t)$. Thus, multiplying equations (8.13) and (8.14) by a_k^* and a_k , respectively, and using this identity, we arrive at the *raw Maxwell-Bloch equations*:

$$\partial_t \rho_{jk} = -i(\omega_j - \omega_k) \rho_{jk} + \frac{i}{\hbar} \mathbf{E}(t) \cdot \sum_{l=1}^N (\mathbf{p}_{jl} \rho_{lk} - \mathbf{p}_{lk} \rho_{jl}) \quad (8.15)$$

To reduce the number of degrees of freedom of (8.15) to a manageable size, we retain only the terms that are in resonance with the material frequencies; *e.g.* those associated with electronic, vibrational and rotational transitions. Additionally, we invoke the *rotating wave approximation* [1] which ignores rapidly oscillating terms. However, due to the presence of weak (non-linear) coupling among the degrees of freedom, there exists many off-resonant terms that are neglected in the above simplifications that in fact have a cumulative effect upon the mode dynamics of the system. This effect is referred to as *homogeneous broadening* and results in a dissipation of energy from the resonant modes analogous to the presence of a heat bath in thermodynamics. To account for this loss in the modeling equations, decay terms of the form $-\gamma_{ij} \rho_{ij}$ are introduced. By so doing, we arrive at the *reduced Maxwell-Bloch equations*

$$\partial_t \rho_{jk} = -(\gamma_{jk} + i\omega_{jk}) \rho_{jk} + \frac{i}{\hbar} \mathbf{E}(t) \cdot \sum_{l=1}^{N'} (\mathbf{p}_{jl} \rho_{lk} - \mathbf{p}_{lk} \rho_{jl}); \quad (8.16)$$

where $\omega_{ij} \equiv \omega_j - \omega_k$ is the *detuning* and the upper index N' is the number of resonant terms retained.

From Maxwell's equations, the macroscopic system variables consisting of the laser cavity field \mathbf{E} and material's responding polarization field \mathbf{P} are governed by

$$\nabla^2 \mathbf{E} - \frac{1}{c^2} \partial_t^2 \mathbf{E} - \nabla(\nabla \cdot \mathbf{E}) = \frac{1}{\epsilon_0 c^2} \partial_t^2 \mathbf{P}. \quad (8.17)$$

where c and ϵ_0 represent the speed of light in vacuum and the permittivity of free space, respectively. Defining the atomic number density n_a to denote the number of interacting atoms, equations (8.16) and (8.17) are coupled through the quantum expectation of the polarization prescribed by equation (8.9)

$$\mathbf{P} = n_a \text{Tr}(\mathbf{p}\rho) = n_a \sum \mathbf{p}_{jk} \rho_{kj}, \quad (8.18)$$

and together constitute the reduced Maxwell–Bloch equations modeling the interaction of light with matter.

To arrive at the Maxwell-Bloch system (3.1), we consider the field variables \mathbf{E} and \mathbf{P} as divergence free, *i.e.* $\nabla \cdot \mathbf{E} = 0$, wavepackets possessing bandwidths $\delta\omega$ about a central carrier mode (\mathbf{k}_0, ω_0) subject to the constraint $\epsilon \equiv \delta\omega/\omega_0 \ll 1$. Accordingly, we write the general solution to (8.17) to leading order in ϵ as

$$\mathbf{E} = \Psi(\mathbf{r}, t) \exp(i(\mathbf{k}_0 \cdot \mathbf{r} - \omega_0 t) + c.c.) \mathbf{e} + \mathcal{O}(\epsilon), \quad (8.19)$$

$$\mathbf{P} = \Lambda(\mathbf{r}, t) \exp(i(\mathbf{k}_0 \cdot \mathbf{r} - \omega_0 t) + c.c.) \mathbf{e} + \mathcal{O}(\epsilon). \quad (8.20)$$

For singly polarized and unidirectional waves, $\mathbf{e} = (0, 1, 0)$ and $\mathbf{k} = (0, 0, \omega/z)$, respectively; Thus, the above wavepacket solutions become

$$\mathbf{E}(\mathbf{r}, t) = \left(\Psi(x, y, t) \exp\left(i\left(\frac{\omega}{c}z - \omega t\right)\right) + c.c. \right) \mathbf{e}, \quad (8.21)$$

$$\mathbf{P}(\mathbf{r}, t) = \left(\Lambda(x, y, t) \exp\left(i\left(\frac{\omega}{c}z - \omega t\right)\right) + c.c. \right) \mathbf{e}; \quad (8.22)$$

After insertion of these waveforms into (8.17), we assume that the envelopes are slowly varying function of both space and time. This assumption implies $\partial_\zeta^n \sim \mathcal{O}(\epsilon^n)$, where $\zeta \in \{x, y, z, t\}$. Hence, to leading order in ϵ , we can set the second order temporal derivatives to zero. Additionally, the assumption of singly polarized

polarization allows the first order temporal derivative of $\Lambda(x, z, t)$ to also be set to zero to produce

$$\left(\partial_z + \frac{1}{c}\partial_t\right)\Psi(x, y, t) = \frac{2i\omega}{c}\partial_x^2\Psi(x, y, t) + \frac{i\omega}{2\epsilon_0 c^2}\Lambda(x, y, t). \quad (8.23)$$

Following Newell, we finally introduce a loss term $-(\kappa/c)\Psi(z, t)$ to characterize the linear system loss and thereby arrive at the Maxwell-Bloch field equation

$$\left(\partial_z + \frac{1}{c}\partial_t\right)\Psi(z, t) = i\frac{c}{2\omega}\partial_x^2\Psi(z, t) - \frac{\kappa}{c}\Psi(z, t) + \frac{i\omega}{2\epsilon_0 c}\Lambda(z, t), \quad (8.24)$$

This is equation (3.1).

To arrive at equations (3.2) and (3.3), we assume two-level atoms and relate the macroscopic polarization field variable to the quantum observables via (8.18)

$$\mathbf{P} = n_a (\mathbf{p}_{12}\rho_{12} + \mathbf{p}_{21}\rho_{21}). \quad (8.25)$$

Furthermore, we follow Newell and define the *inversion density* $N(z, t)$ in terms of the difference between the transition elements

$$N(t) = n_a(\rho_{22} - \rho_{11}). \quad (8.26)$$

Taking the direction of the dipole moments to be parallel to the electric field, we restrict \mathbf{p} to be real and $\mathbf{p}_{12} = \mathbf{p}_{21} \equiv \mathbf{p}e$. Thus from (8.22) and (8.25) we identify

$$n_a p \rho_{12} = \Lambda(x, y, t) e^{i\left(\frac{\omega}{c}z - \omega_0 t\right)}. \quad (8.27)$$

The reduced Bloch equation (8.16) therefore gives

$$\partial_t \rho_{12} = -(\gamma_{12} + i\omega_{12})\rho_{12} + \frac{iE\mathbf{p}}{\hbar}(\rho_{22} - \rho_{11}). \quad (8.28)$$

Combining equations (8.26), (8.27), (8.28) and recalling $\Psi = E \exp(-i((\omega/c)z - \omega t))$, we arrive at

$$\partial_t \Lambda = -(\gamma_{12} + i(\omega_{12} - \omega))\Lambda + \frac{ip^2}{\hbar} \Psi N. \quad (8.29)$$

This is equation (3.3).

To derive the Maxwell-Bloch equation for the inversion density we utilize the reduced Maxwell-Bloch equation twice to arrive at

$$\partial_t \rho_{11} = -\gamma_{11} \rho_{11} + \frac{iE}{\hbar} (p_{12} \rho_{21} - p_{21} \rho_{12}), \quad (8.30)$$

$$\partial_t \rho_{22} = -\gamma_{22} \rho_{22} + \frac{iE}{\hbar} (p_{21} \rho_{12} - p_{12} \rho_{21}). \quad (8.31)$$

Thus, taking $\rho_{21} = \rho_{12}^*$ and $\gamma_{11} = \gamma_{22}$, the difference between (8.31) and (8.30) gives

$$\partial_t (\rho_{22} - \rho_{11}) = -\gamma_{11} (\rho_{22} - \rho_{11}) + \frac{2iEp}{\hbar} (\rho_{12} - \rho_{12}^*). \quad (8.32)$$

Invoking (8.26) and noting $\Psi^* = E \exp(i((\omega/c)z - \omega t))$ thereby produces the final Maxwell-Bloch equation

$$\partial_t N = -\gamma_{11} N + \frac{2i}{\hbar} (\Psi^* \Lambda - \Psi \Lambda^*). \quad (8.33)$$

Finally, introducing a source term $\gamma_{11} N_0$ to account for the external pump that maintains the inversion in the gain results in

$$\partial_t N = -\gamma_{11} (N - N_0) + \frac{2i}{\hbar} (\Psi^* \Lambda - \Psi \Lambda^*). \quad (8.34)$$

This is equation (3.2).

8.2 Map on Integrals and Fluence Code

This section lists the MATLAB code used to generate the stable and unstable manifolds in the phase space of the reduced map on the the saturation integrals and fluence (6.19) discussed in Section 6.2. The code calls the function *trans_3d.m* (provided in Section 8.2.1 below) to numerically determine the roots to the fixed point equation for a given parameter set (g, l, θ, γ_g) as discussed in the thesis. The code is initialized by iterating on ϵ -balls of either normally or uniformly distributed random initial conditions centered on the fixed point of interest. There is one ϵ -ball for each manifold with the radii set by the code variables *eps_unstable* and *eps_stable*. To determine the unstable manifold, the map is simply iterated forward in time; to sample the unstable manifold, the inverse map was first determined and then iterated forward. As a consequence, the unstable manifold of this inverse map is the stable manifold for the original forward map.

The code also calculates the eigenvalues of the Jacobian for each parameter set as well as the condition numbers for each eigenvalue.

```
%SLOW_MAP_3D.M 3-D laser map on fluence and sat. integrals0.
%
%           Produces stable and unstable maifolds in the
%           phase space.

% ----- Code Variables
% r = refletive losses
% rg,rl = gain and loss rates
% tau = round-trip time
% theta = b/a (ratio of stauration parameters)
% Ms = number of initial conditions for stable manifold
% Mu = number of initial conditions for unstable manifold
```

```

% eps_stable = distance from fixed point for initial
%           conditions for stable manifold
% eps_unstable = distance from fixed point; unstable manifold
% iter = iterations for unstable manifold (forward map)
%           The stable manifold loops are controled by stability
%           conditons.
% select_rt = unstable fixed point seed for x3 in
%           transcendental equation
% xfp = fixed point vector
% e = numerical error in fixed points

% ===== Matlab Options =====
clear
format compact

% ===== Parameters =====
global rs theta g l alpha % --- Needed for 3dtrans.m

% ***** Computational (control) Parameters *****
Ms=500; % --- stable manifold.
Mu=50; % --- unstable manifold.
eps_stable=1e-3;
eps_unstable=1e-1;
iter=500;

% ***** Model Parameters *****

```

```

% NOTES: Interactive Option: To in-put parameters, remove
%       comment symbol on "while" statement and its
%       associated "end" statement below as well as the
%       "select_rt" initialization and parameter variables;
%       input statments including select_rt are located below.

%select_rt=0;

%while select_rt == 0
% in=input('Enter [g,l,theta] vector: ')
% g=in(1); l=in(2); theta=in(3);

% NOTES: For default values that provide bistability,
%       comment-out dist(...), theta, g, l and
%       select_rt here.

disp('Defaults parameters are, [theta,g,l]=[50.0,0.06,0.062];...
      root seed = 1.5')
theta=50.;g=0.06;l=0.062;
select_rt=1.5; % --- Unstable fixed point seed for x3 in
               %      transcendental eqn. for these defaults.

% ----- Fixed Physical Parameters
r=0.98;rs=r^2;rg=.25; rl=1; tau=1.25;
alpha=exp(-rg*tau);

% ----- Parameter Dependant Constants
amin1=alpha-1; tamin1=theta*amin1;
cx4=1/tamin1; den1=1-cx4;

```

```

% ***** Fixed Points (from Roots_5d.m) *****

% ----- Plot code for transcendental function on x3 to
%          obtain reasonable root seed for fzero
n=1;
for x3=0:.01:15
    trans_fpe(n)=r^2*(x3+ 2*(g*theta*log(1+x3/(theta*(1-...
        alpha*x3*cx4)) -1*log(1+x3)))-x3;
    t(n)=x3;
    n=n+1;
end
plot(t,trans_fpe), xlabel('x3'), ylabel('h(x3)'),...
        title('3D Transcendental Function'), grid on,

% --- Interactive option for seed determinatin code ending.
%     select_rt=input('Enter initial guest from plot above. If
%     not 0, enter 0: ');
%end

% ----- Numerically determine roots of transcendental fixed
%     point eqn. to form fixed point vector: xfp using
%     seed "select_rt".
x2fp=fzero('trans_3d',select_rt);
x3fp=-x2fp/tamin1;
x1fp=x3fp;
disp('Fixed points: '), xfp=[x1fp x2fp x3fp],

```

```

% ----- Errors in fixed points
e1=x1fp-(x2fp/theta+alpha*x3fp);
    h1=1+x2fp/(theta*(1+alpha*x3fp));
    h2=1+x2fp;
e2=x2fp-rs*(x2fp+2*g*theta*log(h1)-2*l*log(h2));
e3=x3fp-x1fp;
disp('Numerical errors in fixed points: '), e=[e1,e2,e3],

% ***** Initial conditions *****
% ---- Stochastically distributed initial value matrix, x0,
%       is set here; rows are perturbations about the unstable
%       fixed point with each column containing a different
%       initial state of the 3-tuple, xfp.
% NOTES: size(xfp,2)= # columns in xfp vector
%       randn(N,M) gives a normally distributed NxM matrix
%       rand(N,M) gives a uniform.

a = -1; b = 1; % --- Range for stochastic variables
rmatrix_u=a+(b-a)*rand(size(xfp,2),Mu);
nru=rmatrix_u/max(max(abs(rmatrix_u))); % --- Normalized
rmatrix_s=a+(b-a)*rand(size(xfp,2),Ms);
nrs=rmatrix_s/max(max(abs(rmatrix_s)));
x0u=xfp'*ones(1,Mu)+eps_unstable*nru;
x0s=xfp'*ones(1,Ms)+eps_stable*nrs;

n=1;

```

```

% ===== Foward Map Iteration: Unstable Manifold =====
for m=1:Mu      % --- Initial condition loop
    x1(1,m)=x0u(1,m); x2(1,m)=x0u(2,m); x3(1,m)=x0u(3,m);
    for n=1:iter % --- Iteration loop
        x1(n+1,m)=x2(n,m)/theta+alpha*x3(n,m);
        h1=1+x2(n,m)/(theta*(1+alpha*x3(n,m)));
        h2=1+x2(n,m);
        x2(n+1,m)=rs*(x2(n,m)+2*g*theta*log(h1)-2*1*log(h2));
        x3(n+1,m)=x1(n,m);
    end
end

% ===== Inverse Map Iteration: Stable Manifold =====
c1=theta*rs; % --- Parameter Dependant Constants
diff= -.99;
for m=1:Ms % --- Initial condition loop
    ix1(1,m)=x0s(1,m); ix2(1,m)=x0s(2,m); ix3(1,m)=x0s(3,m);...
        ix3(2,m)=x0s(3,m);
    for n=1:iter
        if diff > -1 & ix1(n,m) >=0 & ix2(n,m) >= 0 & ix3(n,m)...
            >=0 & ix1(n,m) < max(max(x2))
                diff=(ix1(n,m)-ix2(n,m)/c1);
                ih1=1+ix2(n,m)/(c1*(1+diff));
                f2=2*(g*theta*log(ih1)-1*log(1+ix2(n,m)/rs));
                ix1(n+1,m)=ix3(n,m);
                ix2(n+1,m)=ix2(n,m)/rs - f2;
                ix3(n+1,m)=(1/alpha)*(ix1(n,m)+(f2-ix2(n,m))/c1);
            end
        end
    end
end

```

```

else
    break
end
end
end

% ===== Graphics =====

az=77;el=36;
figure % --- Initial ball: Unstable Manifold
plot3(x1fp,x2fp,x3fp,'rp','MarkerSize',25),
hold on,
plot3(x0u(1,:),x0u(2,:),x0u(3:),'r.'), view(77,el),...
    xlabel('x1'), ylabel('x2'), zlabel('x3')...
    title('Initial Conditions: Unstable Manifold'), grid on,

figure % --- Initial ball: Stable Manifold
plot3(x1fp,x2fp,x3fp,'rp','MarkerSize',25),
hold on,
plot3(x0s(1,:), x0s(2,:), x0s(3:),'b.'), xlabel('x1'),...
    ylabel('x2'), zlabel('x3'), title('Initial...
    Conditins: Stable Manifold'), grid on, view(az,el)

figure % --- Phase space: Unstable Manifold
plot3(x1fp,x2fp,x3fp,'rp','MarkerSize',25),
hold on,
plot3(x1,x2,x3,'.'), xlabel('x1'), ylabel('x2'),...

```



```

        xlabel('x3'), grid on, title('Unstable Manifold'),...
        view(az,el)

figure % --- Phase space: Stable Manifold
plot3(x1fp,x2fp,x3fp,'rp','MarkerSize',25), view(az,el)
hold on,
plot3(ix1,ix2,ix3,'.' ), xlabel('x1'), ylabel('x2'),...
        xlabel('x3'), grid on, title('Stable Manifold')

figure % --- Phase space: Complete Manifold
plot3(x1fp,x2fp,x3fp,'gp','MarkerSize',25),view(az,el)
hold on
plot3(ix1,ix2,ix3,'b.' ),
hold on,
plot3(x1,x2,x3,'r.' ), xlabel('x1'), ylabel('x2'),...
        xlabel('x3'), grid on, title('Complete Manifold'),...
        view(az,el)

disp('Nous finison')

```

8.2.1 Fixed point MATLAB function

This MATLAB routine is called by *slow_map_3d.m* and is passed to MATLAB's *fzero* function to determine the zeros of equation (6.13).

```

\%TRANS_3D Function script for the transcendental fixed point equation
\%          for the linearized 3d-map on fluence and saturation integrals.

```

```
function x3=trans(x)
global rs theta g l alpha
x4=1/(theta*(alpha-1));
x3=rs*(x+ 2*(g*theta*log(1+x/(theta*(1-alpha*x*x4)))-...
    l*log(1+x)))-x;
```

BIBLIOGRAPHY

- [1] J. Herrmann and B. Wilhelmi. *Lasers for Ultrashort Light Pulses*. North-Holland, Amsterdam, The Netherlands, 1987.
- [2] H. A. Haus. Mode locking of lasers. *IEEE J. on Selected Topics in Quantum Electronics*, 6, 2000.
- [3] B.S. Kerner and V.V. Osipov. *Autosolitons: A New Approach to Problems of Self-Organization and Turbulence*. Kluwer Academic Publishers, Boston, 1994.
- [4] B. A. Malomed, A. G. Vladimirov, G.V. Khodova, and N. N. Rozanov. Stable autosolitons in dispersive media with saturable gain and absorption. *Phys. Lett. A*, 274, 2000.
- [5] B. A. Malomed and H. G. Winful. Stable solitons in two-component active systems. *Phys. Rev. E*, 53:5365, 1996.
- [6] S.V. Fedorov, N. N. Rozanov, and A. G. Vladimirov. Autosolitons in bistable lasers of the b class. *Optics and Spectroscopy*, 85:986, 1998.
- [7] N. N. Rozanov and S.V. Fedorov. Autosolitons in single-mode optical waveguides with nonlinear gain and absorption. *Optics and Spectroscopy*, 84:767, 1998.
- [8] G. H. C. New. Pulse evolution in mode-locked quasi-continuous lasers. *IEEE J. Quantum Electron*, QE-10:115, 1974.
- [9] A. Newell and J. Moloney. *Nonlinear Optics*. Addison-Wesley, Redwood City, USA, 1992.
- [10] H. A. Haus. Theory of mode locking with a slow saturable absorber. *IEEE J. Quantum Electron*, QE-11:763, 1975.
- [11] W.E. Cooke and W. Yang. Private communication.

- [12] G. Steinmeyer, D. H. Sutter, L. Gallmann, and U. Keller N. Matuschek. Frontiers in ultrashort pulse generation: Pushing the limits in linear and nonlinear optics. *Science*, 286:1507, 1999.
- [13] Irl N. Duling, editor. *Compact Sources of Ultrashort Pulses*. Cambridge University Press, Cambridge, England, 1995.
- [14] C. C. Lin and L. A. Segel. *Mathematics Applied to Deterministic Problems in the Natural Sciences*. SIAM–Macmillan Publishing, New York, 1974.
- [15] K. Ikeda and H. Daido. Optical turbulence: Chaotic behavior of transmitted light from a ring cavity. *Phys. Rev. Letters*, 45, 1980.
- [16] J. Guckenheimer and P. Holmes. *Nonlinear Oscillations, Dynamical Systems and Bifurcations of Vector Fields*. Springer-Verlag, New York, USA, 1983.
- [17] W. Yang. Ph.D. Thesis, College of William and Mary.
- [18] E. R. Tracy, X. Z. Tang, and C. Kulp. Takens-bogdanov random walks. *Phys. Rev. E*, 57, 1998.
- [19] E. R. Tracy and X. Z. Tang. Anomalous scaling behavior in takens-bogdanov bifurcations. *Phys. Rev. E*, 57, 1998.
- [20] S. Wiggins. *Introduction to Applied Nonlinear Dynamical Systems and Chaos*. Springer-Verlag, New York, USA, 1991.

VITA

George A. Andrews Jr.

George A. Andrews Jr. was born in Camden New Jersey, on 10 October 1956; attended John F. Kennedy High School in Willingboro N.J. and received the Bachelor of Arts degree in physics from Rutgers University in Camden N.J. in May 1984. In 1986, George earned the Master of Arts degree in physics from Wesleyan University in Middletown Connecticut and then gained professional experience over the following twelve years as a Research Scientist for Scientific Research Associates in Glastonbury CT, and as an Associate Professor of Physics and Chairman of the Natural Science Department at LeTourneau University in Longview Texas. George entered the Applied Science Department of the College of William and Mary in Virginia in September 1998. This dissertation was defended on 4 December 2000 at the College of William and Mary in Virginia.